nature cell biology

Endoglin controls blood vessel diameter through endothelial cell shape changes in response to haemodynamic cues

Wade W. Sugden[1,2], Robert Meissner[2,3], Tinri Aegerter-Wilmsen[4], Roman Tsaryk[1,2], Elvin V. Leonard[1,2], Jeroen Bussmann[1,7], Mailin J. Hamm[1,2,5], Wiebke Herzog[1,2,5], Yi Jin[6], Lars Jakobsson[6], Cornelia Denz[2,3] and Arndt F. Siekmann[1,2,8]

The hierarchical organization of properly sized blood vessels ensures the correct distribution of blood to all organs of the body, and is controlled via haemodynamic cues. In current concepts, an endothelium-dependent shear stress set point causes blood vessel enlargement in response to higher flow rates, while lower flow would lead to blood vessel narrowing, thereby establishing homeostasis. We show that during zebrafish embryonic development increases in flow, after an initial expansion of blood vessel diameters, eventually lead to vessel contraction. This is mediated via endothelial cell shape changes. We identify the transforming growth factor beta co-receptor endoglin as an important player in this process. Endoglin mutant cells and blood vessels continue to enlarge in response to flow increases, thus exacerbating pre-existing embryonic arterial–venous shunts. Together, our data suggest that cell shape changes in response to biophysical cues act as an underlying principle allowing for the ordered patterning of tubular organs.

Networks of tubular epithelia are important for the transport of liquids and gases throughout the body[1]. The hierarchical order of these networks is an important prerequisite for their correct function. Within the vasculature, a rise in metabolic demand of the brain or muscle tissue leads to vasodilation and an increase in blood flow[2,3]. In turn, changes in blood flow can influence blood vessel sizes. Previous studies showed that higher flow rates induce an increase in vessel diameter via outward remodelling, while lower shear stress levels lead to a decrease in blood vessel size via inward remodelling[4–9]. Together, these observations supported the theory of a shear stress set point for the endothelium, with inward and outward remodelling ensuring constant shear rates within blood vessels and therefore homeostasis[10–12]. Despite the attractiveness of this concept, Thoma already noted in 1893 that the unrestricted flow-driven increase of blood vessel diameters during embryonic development would ultimately lead to a situation where two massive blood vessels carry all of the systemic flow[13]. This phenomenon was later referred to as the shunt problem[14]. Arteriovenous malformations (AVMs) are characterized by enlarged direct connections between arteries and veins bypassing an intervening capillary bed, leading to blood flow shunting. Mutations in the transforming growth factor beta (TGF-beta) pathway components *alk1* or *endoglin* (*eng*) are associated with AVM formation in mouse and humans, where they cause hereditary haemorrhagic telangiectasia (HHT)[15]. While mutations in zebrafish *alk1* cause AVM formation[16], no zebrafish *eng* gene has been identified so far. Earlier work showed that an increase in endothelial cell (EC) numbers within AVMs leads to blood vessel enlargement and flow shunting[16–19]. However, the precise temporal events of AVM formation and the functions of *alk1* and *eng* in integrating haemodynamic cues with different tube sizes remain poorly understood.

Adult zebrafish *eng* mutants display vascular malformations

To investigate the mechanisms controlling blood vessel diameters we set out to identify and functionally characterize the zebrafish homologue of *ENG*. Since database searches failed in identifying zebrafish *eng*, we employed a synteny-based approach (Supplementary Fig. 1a; see Methods). Sequence analysis of the identified gene predicted a protein product of similar length to human *ENG* (Supplementary Fig. 1b).

[1]Max Planck Institute for Molecular Biomedicine, Roentgenstrasse 20, D-48149 Muenster, Germany. [2]Cells-in-Motion Cluster of Excellence (EXC 1003 – CiM), University of Muenster, D-48149 Muenster, Germany. [3]Institute of Applied Physics and Center for Nonlinear Science (CeNoS), University of Muenster, D-48149 Muenster, Germany. [4]Institute of Molecular Life Sciences, University of Zurich, Winterthurerstrasse 190, 8057 Zurich, Switzerland. [5]University of Muenster, D-48149 Muenster, Germany. [6]Karolinska Institute, Department of Medical Biochemistry and Biophysics, SE 171 77 Stockholm, Sweden. [7]Present address: Department of Supramolecular & Biomaterials Chemistry, Leiden Institute of Chemistry (LIC), Gorlaeus Laboratories, Leiden University, PO Box 9502, 2300 RA Leiden, The Netherlands.
[8]Correspondence should be addressed to A.F.S. (e-mail: arndt.siekmann@mpi-muenster.mpg.de)

Received 19 July 2016; accepted 7 April 2017; published online 22 May 2017; DOI: 10.1038/ncb3528

In addition, phylogenetic analysis of the cytoplasmic domain placed this gene within the endoglin clade (Supplementary Fig. 1c). Together with a recent report[20], our analysis also suggests that a previously described zebrafish *eng* gene[21] more likely belongs to the TGF-beta receptor type 3 (betaglycan) gene family. *In situ* hybridization to detect *eng* messenger RNA in developing zebrafish embryos revealed vascular-restricted expression (Supplementary Fig. 1d), similar to *eng* expression in mice[22] and humans[23]. In addition, blocking blood flow reduced *eng* expression within a subset of ECs (cells of the dorsal longitudinal anastomotic vessel; Supplementary Fig. 1e). A similar regulation of endoglin expression via blood flow had been previously reported in mice[24]. Therefore, protein structure, vascular-restricted expression and regulation via shear stress suggest that we identified a zebrafish *ENG* homologue.

We then employed transcription activator-like effector nuclease (TALEN)-mediated mutagenesis to disrupt *eng* function. We generated 3 different mutant alleles, 2 of which led to a frameshift after 15 amino acids (aa) and premature stop codons after 61 aa (Fig. 1a). Expression of *eng* mRNA containing frameshift mutations (*mu130* allele) was reduced, as analysed via quantitative PCR (qPCR; Supplementary Fig. 2a) and *in situ* hybridization (Supplementary Fig. 2b, arrows), together suggesting that we have very likely generated *eng* loss of function alleles. Surprisingly, in contrast to *Eng* homozygous mutant mice, which die during embryogenesis[22], homozygous *eng* mutant zebrafish survived into adulthood (Fig. 1b). Closer examination of the brain vasculature revealed the presence of multiple vascular malformations characterized by tortuous and regionally enlarged blood vessels (Fig. 1c,d, yellow arrowheads). Since vascular malformations in HHT are often detected in regions of active angiogenesis[15], we decided to investigate blood vessel morphogenesis in a neoangiogenesis setting, the regenerating zebrafish fin[25] (Fig. 1e).

Amputation of wild-type fins resulted in the formation of a distally located vascular plexus, which received blood flow from the artery (Fig. 1f,g). Occasionally (3/89 cases), we observed aberrant blood flow patterns in the regenerate with arteries lacking blood flow (Supplementary Video 1). The frequency of these malformations was greatly increased in *eng* homozygous mutants (49/86 cases; Supplementary Video 2). We detected blood pooling in dilated vessels and blood flow patterns that resembled AVMs with arterial flow prematurely draining into veins without irrigating the distally located blood vessel plexus (Fig. 1h,i, ray no. 2). Previous studies implicated increases in EC numbers as the cause for blood vessel enlargement in *Eng* mutants[16–19]. We therefore determined vessel calibres and endothelial cell numbers (Fig. 1j–o). These quantifications revealed increases in vessel diameters both in arteries and veins in homozygous *eng* mutants (Fig. 1l). Surprisingly, EC numbers were increased only in mutant veins (Fig. 1m). Endothelial area was increased in both vessels (Fig. 1n), and consequently cell density decreased in mutant arteries but remained constant in veins (Fig. 1o). Together, these results show that zebrafish *eng* mutants present with enlarged blood vessels that can lead to AVM formation, but partly without increases in endothelial cell numbers.

Mutations in *eng* affect embryonic blood vessel calibres

To examine whether similar vascular malformations also occur during embryonic stages, we examined vascular morphologies in the zebrafish trunk, where angiogenic sprouting generates the intersegmental blood vessels (ISVs)[26]. At 72 hours post fertilization (hpf), wild-type embryos had fully established arterial and venous ISVs, connecting the dorsal aorta (DA) with the posterior cardinal vein (PCV; Fig. 2a). Despite normal blood vessel connectivity in *eng*^{mu130} mutants, we noted a dramatic reduction in blood flow through ISVs (Supplementary Videos 3 and 4). Nearly 50% of mutant ISVs did not carry erythrocytes (Fig. 2b). Angiography revealed that ISVs were properly lumenized (Fig. 2c, arrows). We observed a small but significant dilation of *eng*^{mu130} mutant arterial ISVs (aISV), while venous ISV (vISV) diameters were substantially decreased (Fig. 2d). Mutant aISVs contained similar numbers of endothelial cells when compared to wild-type embryos, whereas vISVs contained marginally fewer cells (Fig. 2e). Thus, a reduction in endothelial cell numbers could explain the decrease in vISV diameters, thereby reducing blood flow. We asked whether the reduced blood flow might cause ISV regression in *eng*^{mu130} mutants, as low blood flow has been shown to cause blood vessel pruning[27,28]. Two weeks after the onset of ISV blood flow (17 days post fertilization time point), we observed pruning of about 20% of ISVs in wild-type embryos (Supplementary Fig. 3a,f), suggesting that the trunk vasculature remodels during this time frame. In *eng*^{mu130} mutant embryos, we did not observe a change in arterial or venous ISVs nor in the amount of ISVs containing red blood cells at this later time point, but twice as many ISVs had remodelled (Supplementary Fig. 3b–f). Hence, loss of *eng* function leads to an increase in blood vessel pruning, possibly as a long-term consequence of altered haemodynamics.

Further evaluation of blood vessel morphologies in 72 hpf embryos showed no change in the ratio of arterial to venous ISVs in *eng*^{mu130} mutants compared to wild-type (Supplementary Fig. 4a,b). However, we observed an increase in the sizes of the DA and PCV in *eng*^{mu130} mutants (Fig. 2a,c, arrowheads, f). Both vessels dilated by approximately 30%, without a change in the number of endothelial cells comprising either the DA or PCV (Fig. 2g). Therefore, in *eng*^{mu130} mutants, most of the trunk blood flow is shunted through a direct connection between the major artery (DA) and vein (PCV) while bypassing smaller ISVs. This flow pattern might resemble those found in AVMs in more mature vascular beds[29]. ISV blood flow could be significantly rescued by transgenic overexpression of EGFP-tagged *eng* in blood vessels (Supplementary Fig. 4c–f), suggesting that the observed phenotypes in *eng*^{mu130} mutants are very likely due to a loss of *eng* function in ECs.

Blood flow patterns adapt to the expansion of the embryonic vasculature

We took advantage of the stereotypic embryonic trunk vasculature to understand the onset of the AVM-like flow phenotype in *eng*^{mu130} mutants, and measured blood vessel diameters over time (Fig. 3a–d). In wild-type embryos, DA and PCV diameters increased between 24 hpf (onset of blood flow) and 48 hpf with the artery always showing a smaller diameter compared with the vein (Fig. 3a,b). This increase in vessel diameters is consistent with an increase in cardiac output and blood flow[30,31]. At 72 hpf, however, diameters of both the DA and PCV decreased[30], while they continued to enlarge in *eng*^{mu130} mutants (Fig. 3c,d). Therefore, while wild-type blood vessels display a biphasic response to increases in blood flow, the second part of this response—blood vessel constriction—is abrogated in *eng*^{mu130}

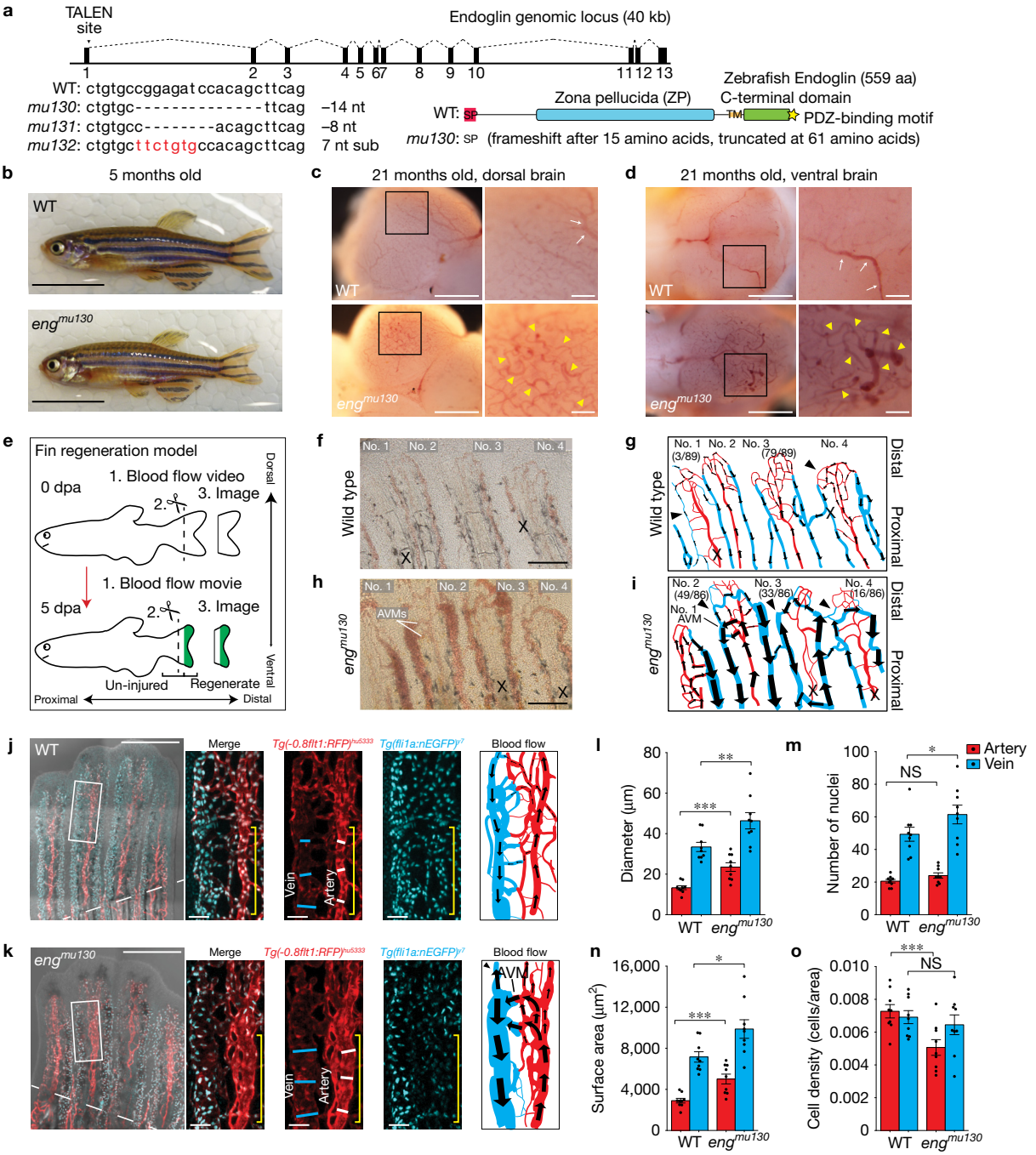

Figure 1 Zebrafish *eng* mutants develop AVMs. (**a**) TALEN target site of zebrafish *eng* and isolated alleles. Endoglin domain structure predicted by zebrafish primary sequence: signal peptide (SP, red), zona pellucida domain (ZP, blue), transmembrane region (TM, orange), cytoplasmic region containing a serine/threonine-rich sequence (green) and a C-terminal PDZ-binding motif (yellow star). (**b**) Adult WT and *eng*^{mu130} zebrafish. Scale bars, 10 mm. (**c**,**d**) Dorsal (**c**) and ventral (**d**) images of dissected brains from aged zebrafish. WTs exhibit hierarchical organization of vasculature, with large calibre vessels (arrows in inset). *eng*^{mu130} zebrafish present with dilated tortuous vessels (arrowheads in inset) and loss of hierarchical patterning. Images are representative of 5 WT and 5 mutant (mut) fish. Scale bars, 500 μm (overview) and 100 μm (inset). (**e**) A schematic of the fin regeneration model (dpa, days post amputation). (**f**–**i**) Still images from blood flow videos in 5 dpa fin regenerate and schematic depiction of blood flow (arrows) in WTs (**f**,**g**) and *eng*^{mu130} mutants (**h**,**i**). Numbers label individual rays in the video. Arrows indicate flow direction; arrowheads highlight reversals. Numbers in parentheses depict number of rays in analysed fish sharing a similar flow characteristic (89 rays from 12 WT, and 86 rays from 12 mut). X indicates large inactive vessel. Note bleedings at distal tips of regenerating rays in *eng*^{mu130} fish. Scale bars, 200 μm. (**j**,**k**) Maximum intensity projections of confocal *z*-stacks of AVM in *eng*^{mu130} regenerate and comparable region in WT at 5 dpa. The dashed line indicates the amputation plane. The solid lines indicate vessel calibre and the yellow bracket indicates the region of vasculature analysed (inset). The schematic depicts the blood flow patterns in the videos. Note shunting of arterial blood to the vein in mutant AVM, and flow reversal in the distal part of the affected vein (arrowhead). Scale bars, 400 μm (overview) and 50 μm (inset). (**l**–**o**) Quantification of diameter (**l**), endothelial cell (EC) number (**m**), endothelial area (**n**) and cell density (**o**) in arteries and veins in proximity to AVM in *eng*^{mu130} fish and comparable WT regions ($n=9$ WT, $n=9$ mut). Analysed by paired Student's *t*-test. NS, not significant; $^{*}P<0.05$, $^{**}P<0.01$, $^{***}P<0.001$; error bars indicate s.e.m.

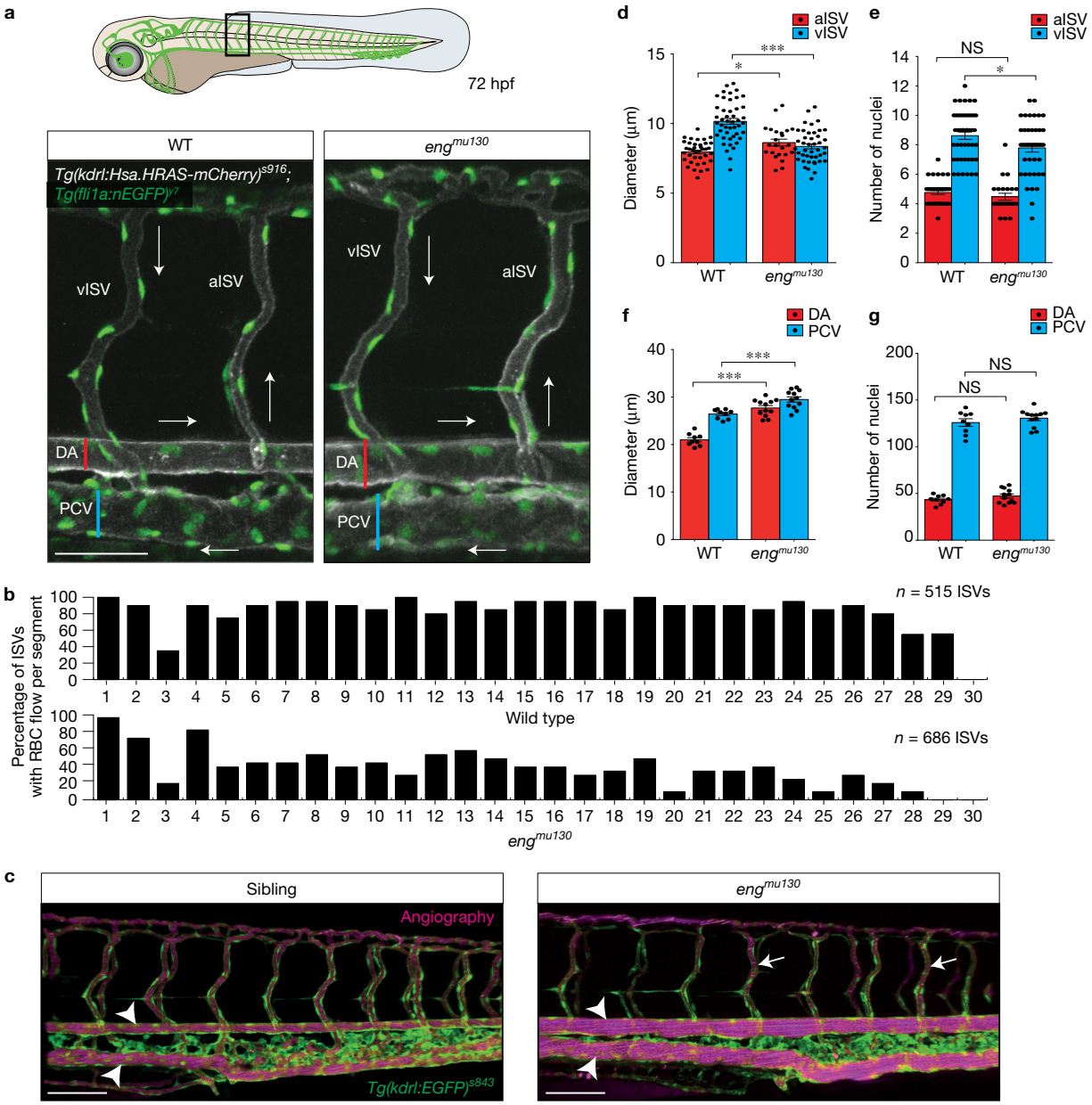

Figure 2 Zebrafish 72 hpf trunk vasculature recapitulates an AVM-like phenotype. (**a**) A schematic of a 72 hpf embryo; the box indicates the region of the images. Maximum intensity projection of a confocal *z*-stack of a single segmental unit in a zebrafish trunk at 72 hpf. *Tg(kdrl:Hsa.HRAS-mcherry)*^{s916} labels EC membranes, while *Tg(fli1a:nEGFP)*^{y7} shows EC nuclei. The dorsal aorta (DA), posterior cardinal vein (PCV), arterial and venous intersegmental vessels (aISVs and vISVs) are labelled. Blood flow direction is indicated with arrows. Scale bar, 60 μm. (**b**) Quantification of the number of ISVs actively carrying RBCs shows approximately 50% reduction in *eng*^{mu130} embryos (515 ISVs from 9 WT embryos, 686 ISVs from 12 mut embryos). (**c**) Angiography with 633 nm quantum dots in *eng*^{mu130} sibling and mutant. Both sibling and mutant embryos show lumenization of nearly all ISVs (arrows). Note, however, the dramatic increase in diameter of axial vessels in the mutant compared with sibling (arrowheads). Images are representative of 6 WT and 6 mut embryos. Scale bars, 100 μm. (**d**) Quantification of vessel diameter for aISVs and vISVs in WT and *eng*^{mu130} mutant embryos. In WTs, vISVs have a larger diameter than aISVs. In mutants, aISVs slightly dilate while vISVs have a reduced calibre ($n = 38$ aISVs/46 vISVs from 9 WTs; $n = 23$ aISVs/43 vISVs from 12 mut). Analysed by unpaired Student's *t*-test. (**e**) Quantification of EC number in ISVs. There is no change in the EC number in aISVs, while vISVs show a slight reduction in EC number. Analysed by Mann–Whitney *U* test ($n = 38$ aISVs/46 vISVs from 9 WTs; $n = 23$ aISVs/43 vISVs from 12 mut). (**f**) Quantification of vessel diameter for the DA and PCV in WT and *eng*^{mu130} mutant embryos. Both DA and PCV show significant dilation in mutants ($n = 9$ WT, $n = 12$ mut). Analysed by unpaired Student's *t*-test. (**g**) Quantification of the number of ECs in the DA and PCV. WT and *eng*^{mu130} mutants have no difference in EC numbers in these vessels ($n = 9$ WT, $n = 12$ mut). Analysed by unpaired Student's *t*-test. NS, not significant; $^{*}P < 0.05$, $^{***}P < 0.001$; error bars indicate s.e.m.

mutants, leading to arteriovenous shunt formation (Fig. 3e–j; Fig. 4a). We next measured blood flow parameters within developing blood vessel shunts using particle image velocimetry[32]. At 48 hpf, wild-type embryos displayed pulsatile blood flow in the DA with a peak velocity of about 2,000 μm s^{-1}, which is in agreement with previous reports[31]. We noted that this pulsatility was transmitted to the venous flow,

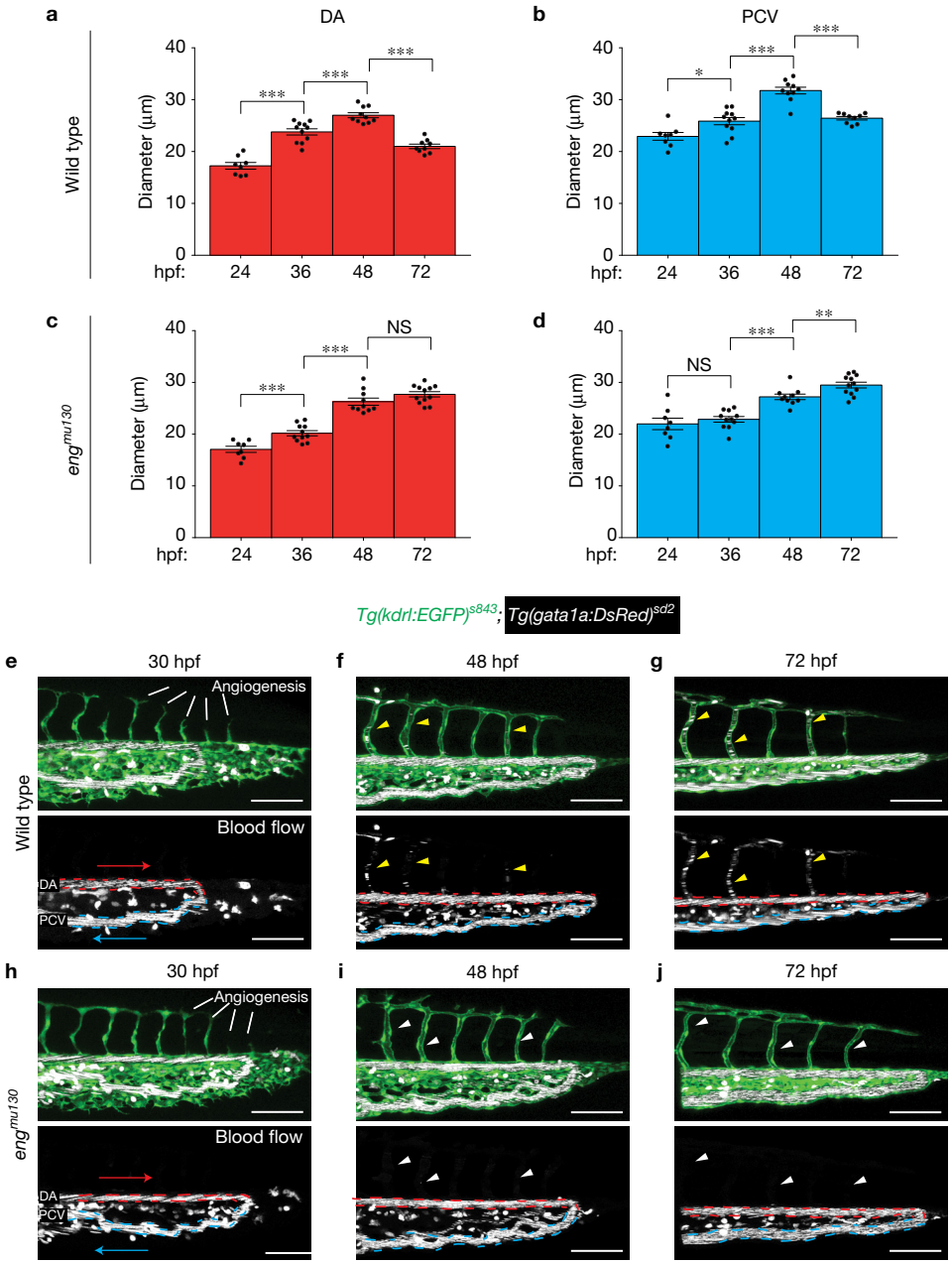

Figure 3 Analysis of DA and PCV diameter during development. (**a**,**b**) Average DA (**a**) and PCV (**b**) diameter in WT embryos from 24–72 hpf. Note the steady increase in vessel calibre until 48 hpf, followed by reduction at 72 hpf. (**c**,**d**) Average DA (**c**) and PCV (**d**) diameter in *eng*^{mu130} embryos from 24 to 72 hpf. The same progression of vascular calibre increases as WT until 48 hpf, with pronounced failure to reduce size at 72 hpf in both artery and vein (WT 24, 36, 48, 72 hpf: $n=8$, 11, 10, and 9 embryos; mut 24, 36, 48, 72 hpf: $n=8$, 11, 10, 12 embryos). Analysed by unpaired Student's *t*-test. (**e**–**j**) Maximum intensity projections of confocal *z*-stacks of WT (**e**–**g**) and *eng*^{mu130} mutants (**h**–**j**) at 30, 48 and 72 hpf. The dashed lines indicate DA (red) and PCV (blue), while the arrows indicate the flow direction. At 30 hpf, the ISV network is still in the process of forming via sprouting angiogenesis, and does not have RBCs in the vessels. In WTs, RBC flow in ISVs is weak at 48 hpf and strongly increased by 72 hpf (yellow arrowheads in **f**,**g**). The white arrowheads (**i**,**j**) show ISVs that are lumenized but do not carry RBCs in *eng*^{mu130} mutants. Images are representative of 6 WT and 6 mut embryos. Scale bars, 100 µm. NS, not significant; $^{*}P<0.05$, $^{**}P<0.01$, $^{***}P<0.001$; error bars indicate s.e.m.

exemplified by peak PCV velocities immediately following arterial peaks (Fig. 4b, 48 hpf time point, arrow). Thus, due to the topology of the initial embryonic circulatory loop, the DA and PCV blood flow profiles resemble those present in arteriovenous shunts. Of note, after the addition of ISVs at the 72 hpf time point, pulsatility within the DA remained constant, while venous pulsatility was reduced (Fig. 4c,f,g), as observed in more mature vascular beds[33]. In addition, maximum velocity was reduced in the PCV, with a similar trend in the DA (Fig. 4h,i). Shear stress was reduced in both the DA and PCV between 48 and 72 hpf (Fig. 4j,k). In *eng*^{mu130} embryos, initial flow profiles at 48 hpf resembled those in wild-type embryos with respect to pulsatility and shear stress, while velocity was reduced (Fig. 4d,f–k). However, at the 72 hpf time point, pulsatility was reduced in the DA, and increased within the PCV (Fig. 4e, arrow, f,g). Furthermore, maximum velocity

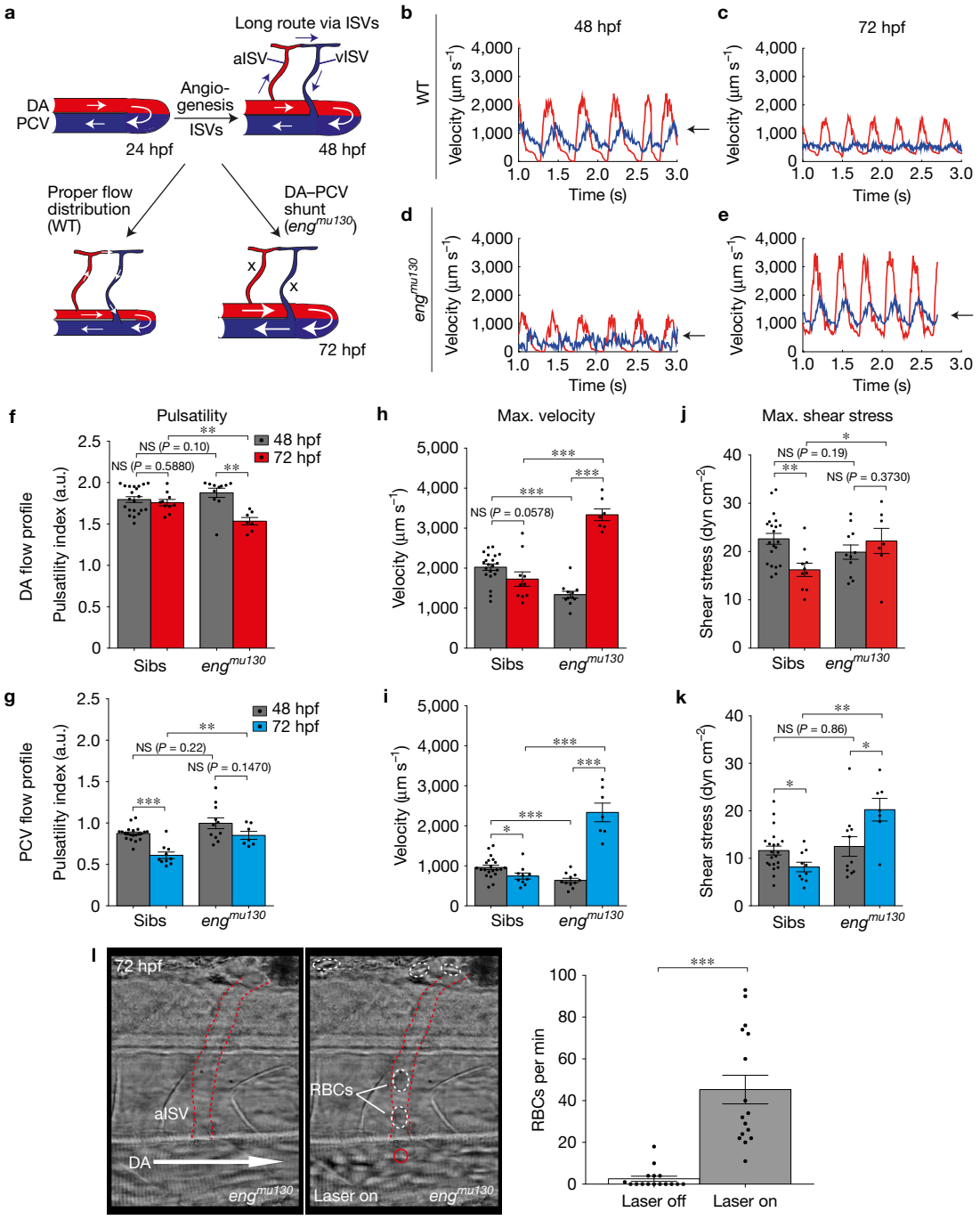

Figure 4 Blood flow patterns adapt to the expansion of the embryonic vasculature. (**a**) A schematic depicting blood flow changes through axial vasculature during development. At 24 hpf, all blood flow is through a primary arterial–venous loop. The addition of new capillaries through angiogenesis creates longer loops that are perfused with RBCs in WT, but not in *eng*^{mu130} mutants. (**b**–**e**) Representative DA (red) and PCV (blue) blood flow profiles for sibling and *eng*^{mu130} mutant embryos at 48 hpf and 72 hpf. Arrows indicate PCV velocity peaks following arterial velocity peaks. (**f**–**k**) Quantification of DA and PCV blood flow parameters (pulsatility, maximum velocity and maximum shear stress) in siblings and *eng*^{mu130} mutants between 48 hpf and 72 hpf (48 hpf $n = 21$ siblings, $n = 11$ mut; 72 hpf $n = 10$ siblings, $n = 7$ mut). Analysed by Mann–Whitney U test. (**l**) Still images from a video showing diversion of RBCs into the aISV by application of holographic optical tweezers (HOT). The arrow indicates the direction of DA blood flow. The aISV is outlined by dashed red lines. The red circle denotes the HOT laser focal point near the aISV entrance. The dashed white circles highlight RBCs in the lumen of the aISV. Quantification of RBC flow through the same ISVs with HOT inactive (laser off) or active (laser on) ($n = 16$ aISVs). Analysed by Mann–Whitney U test. NS, not significant; $^{*}P < 0.05$, $^{**}P < 0.01$, $^{***}P < 0.001$; error bars indicate s.e.m.

and shear stress were increased both in the artery and vein (Fig. 4h–k). Therefore, while wild-type embryos initially display flow profiles that are reminiscent of an arteriovenous shunt, these are rectified after the addition of capillaries via angiogenesis. In *eng*^{mu130} mutants this shunt-like flow becomes exacerbated, leading to dramatic alterations of blood flow profiles.

We hypothesized that the high velocities in *eng*^{mu130} mutant AVMs may hinder red blood cell (RBC) passage through capillaries, and employed holographic optical tweezers[34] at the DA entrance of aISVs in *eng*^{mu130} mutant embryos to slow down RBC movement. This 'optical rail' could divert RBCs from the AVM into aISVs (Fig. 4l and Supplementary Video 5). These findings suggest that haemodynamic changes within the primary axial vessels might prevent capillary RBC perfusion. Therefore, the establishment of aberrant arterial–venous flow patterns in *eng*^{mu130} mutant embryos might be caused by structural changes that occur within primary vessels after the onset of blood flow and not due to defects in angiogenesis or lumen formation in capillaries.

Eng does not affect *klf2a*-mediated shear stress sensing

Our observations show that *eng* mutant blood vessels display aberrant responses to an increase in blood flow. Previous studies showed that ECs align in the direction of shear stress[35] in a *klf2a*-dependent manner[36]. To address whether shear stress sensing was defective in *eng*^{mu130} mutants, we analysed mRNA expression of *klf2a*, which is upregulated in response to shear stress[37]. Surprisingly, *klf2a* was more strongly expressed in the PCV in *eng*^{mu130} mutant embryos (Fig. 5a), consistent with our finding that shear stress is higher in this vessel. To monitor alterations in shear stress within living embryos, we developed a *Tg(klf2a:YFP)*^{mu107} line, which displayed endothelial-specific YFP expression in response to shear stress (Supplementary Fig. 5). Consistent with a decrease in blood flow, we observed downregulation of YFP expression in ISVs in *eng*^{mu130} mutants compared with wild-type embryos (Fig. 5b, arrows, c). There was a trend in mutant embryos toward a decrease in YFP intensity within the DA and an increase in the PCV (Fig. 5b,d). We further knocked down *ENG* in human umbilical vein endothelial cells (HUVEC) exposed to shear stress (Fig. 5e) and analysed the expression of *KLF2* (Fig. 5f) and *CXCR4* (Fig. 5g), a gene reported to be downregulated via shear stress[38]. We again found no change in the response of control or ENG short interfering RNA (siRNA)-transfected ECs to shear stress. Together, these findings suggest that *eng*-deficient ECs do not have a defect in shear stress sensing upstream of *klf2a*, but can even respond to increased shear stress in embryonic blood vessels with an upregulation of *klf2a* expression.

Loss of *eng* function leads to blood vessel enlargement in an EC autonomous manner

We next set out to investigate the cause for the observed DA and PCV dilation. We reasoned that it might be a secondary consequence of vISV constriction, forcing blood flow into the DA and PCV. Alternatively, dilation of the DA and PCV might prevent ISV blood flow, secondarily leading to a decrease in vISV diameters. To distinguish between these possibilities, we performed cell transplantation experiments (Fig. 6a), resulting in situations where either an entire ISV was comprised of donor ECs (Fig. 6b–e) or only parts of a given ISV (Supplementary Fig. 6). Transplanting wild-type ECs to wild-type embryos resulted in similarly sized ISVs (Fig. 6c). By contrast, ISVs entirely comprised of *eng*^{mu130} mutant endothelial cells in an otherwise wild-type vasculature exhibited an almost 80% increase in diameter (Fig. 6d,f). We observed a similar increase in diameter when we analysed mosaic ISVs (Supplementary Fig. 6b,e,g). Transplanting wild-type cells into mutant embryos resulted in a dramatic decrease in lumen diameter in wild-type ISVs (Fig. 6e,f), while mosaic blood vessels showed an intermediate diameter (Supplementary Fig. 6c,f). Together, our transplantation experiments suggest that eng acts in a cell autonomous manner within single ECs and that dilation is a primary consequence of loss of eng function.

Eng function is necessary for blood flow-induced cell shape changes

We reasoned that changes in EC shapes and not numbers might lead to the observed alterations in tube dimension. To address this question, we stained 72 hpf wild-type and mutant embryos for the tight junction protein ZO-1 (Fig. 7a). Endothelial cells in wild-type embryos at 72 hpf showed elongated ECs that were arranged in an orderly, cobblestone-like fashion. In contrast, ECs in *eng*^{mu130} embryos showed a disordered DA assembly, with apparently larger ECs. To visualize the architecture of ECs in living fish, we utilized a *Tg(fli1a:lifeactEGFP)*^{mu240} line together with *Tg(-0.8flt1:RFP)*^{hu5333} and *Tg(fli1a:nEGFP)*^{y7}. Lifeact-EGFP has been shown to be enriched at cell–cell contacts[39], while we observed mosaic expression of *Tg(-0.8flt1:RFP)*^{hu5333} in the axial vasculature. In combination, these lines enabled us to distinguish single ECs and quantify their morphologies (Fig. 7b–g). In 48 hpf wild-type embryos, ECs within the DA showed a rounded morphology (Fig. 7d) and were moderately aligned in the direction of blood flow, as measured by the cell angle in relation to the blood vessel (Fig. 7e). At 72 hpf, wild-type cells were more elongated and aligned, while keeping their surface areas and perimeters constant (Fig. 7d–g). In effect, these cell shape changes within a tube would lead to a more narrow and elongated tube, as also evidenced by time-lapse imaging (Supplementary Video 6). Therefore, our results show that endothelial cell shape changes between 48 and 72 hpf cause a decrease in DA diameter in wild-type embryos.

The morphology of *eng*^{mu130} mutant ECs did not differ from wild-type ECs at 48 hpf, except for a reduction in surface area (Fig. 7d–g). However, at 72 hpf we observed a drastic increase in surface area of about 30% (Fig. 7f). Mutant ECs elongated to the same extent as wild-type cells (Fig. 7d). They also became more aligned to flow over time, but not as well as wild-type cells (Fig. 7e), jointly leading to a less efficient decrease in tube diameter (Supplementary Video 7). These morphometric characteristics are summarized in Fig. 7h. Together, our results show that the increase in blood vessel diameters in *eng*^{mu130} mutants is caused by an increase in EC surface areas and aberrant changes in EC shapes.

Due to the reported function of blood flow during AVM development[40], we inferred that haemodynamic cues might induce the observed structural changes within ECs. To address this question, we treated zebrafish embryos with 2.25× tricaine from 48 to 72 hpf in order to reduce cardiac output[31]. Tricaine treatment caused a general decrease in EC cell surface areas in both wild-type and *eng*^{mu130} mutants, but with a stronger effect in *eng*^{mu130} mutant embryos (Fig. 7f). Tricaine also eliminated differences in perimeter and angle of ECs between WT and *eng*^{mu130} mutants (Fig. 7e,g). Therefore, blood flow critically influences EC sizes with *eng*^{mu130} mutant ECs showing defects in the response to this biophysical stimulus. We then asked whether similar *eng*-dependent changes in cell size occur in mammalian ECs. We analysed HUVEC in culture and observed EC alignment in the direction of flow as previously published[35].

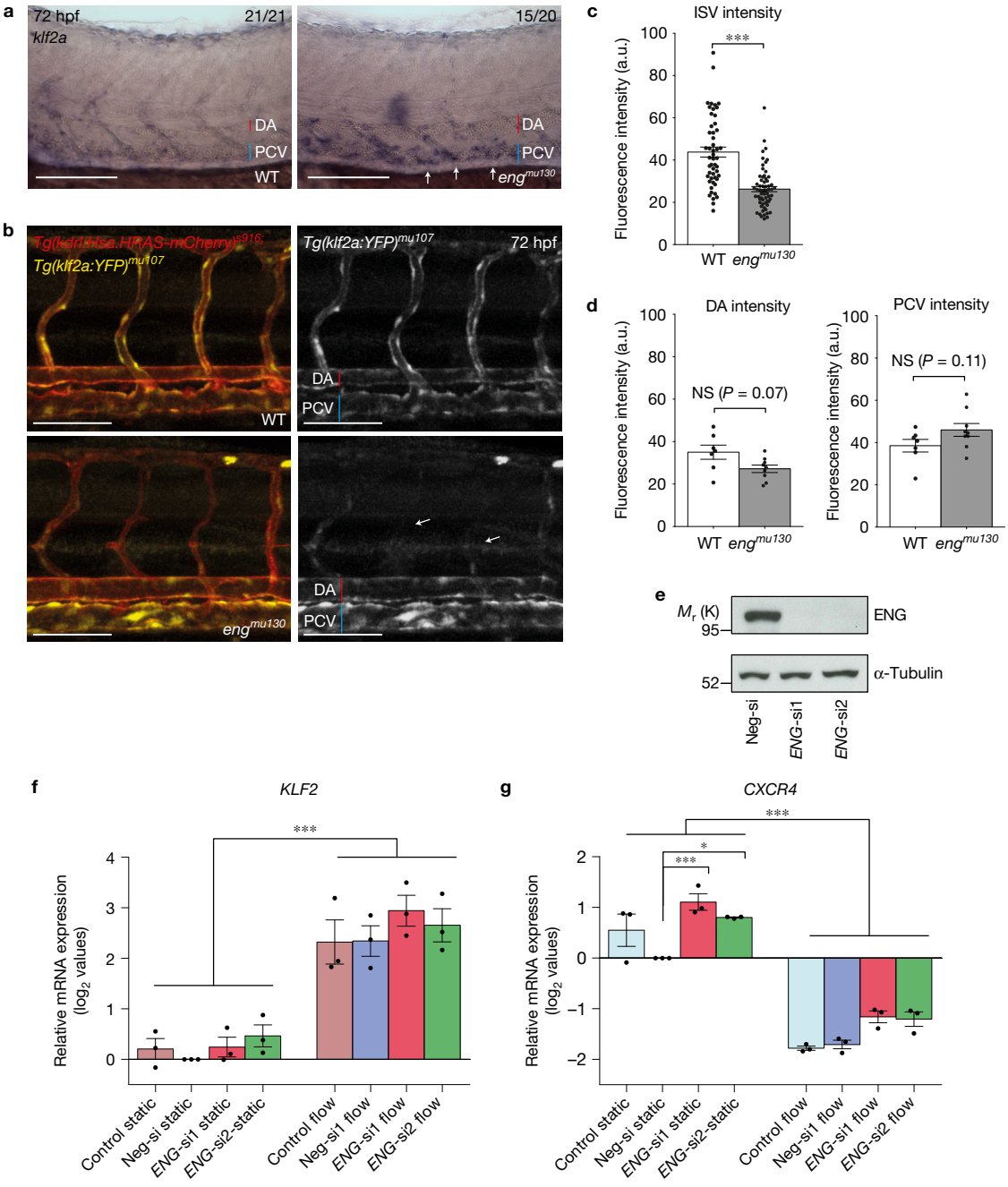

Figure 5 *Eng* does not affect *klf2a*-mediated shear stress sensing. (**a**) Whole-mount *in situ* hybridization of endogenous *klf2a* expression in WT or eng^{mu130} mutant embryos at 72 hpf. Note the enhanced staining in PCV of eng^{mu130} mutants (arrows). Images are representative of 21 out of 21 WT embryos and 15 out of 20 mut embryos. Scale bars, 100 μm. (**b**) Maximum intensity projection of a confocal *z*-stack of a zebrafish trunk at 72 hpf. $Tg(klf2a:YFP)^{mu107}$ exhibits vascular-specific YFP expression, evidenced by overlap with $Tg(kdrl:Hsa.HRAS\text{-}mCherry)^{s916}$. eng^{mu130} mutants also display YFP expression in axial vessels, but decreased expression in ISVs (arrows). Scale bars, 100 μm. (**c**,**d**) Quantification of YFP fluorescence intensity in ISVs, DA and PCV of WT and eng^{mu130} mutants. ISVs have reduced YFP signal, while eng^{mu130} mutants have a trend toward less intensity in the DA and more intensity in the PCV (not significant) (ISVs $n = 51$ ISVs from 7 WT, $n = 62$ ISVs from 9 mut; DA/PCV $n = 7$ WT, $n = 9$ mut). Analysed by Mann–Whitney *U* test. (**e**) Downregulation of ENG in HUVEC. siRNA efficiency was confirmed with western blot (representative of 8 blots is shown, relative molecular mass is shown on the left). Unprocessed original scans of blots are shown in Supplementary Fig. 8. (**f**,**g**) The expression of shear-stress-responsive genes *KLF2* (**f**) and *CXCR4* (**g**) in siRNA-transfected HUVEC exposed to 15 dyn cm^{-2} for 4 h. mRNA expression data are shown as log_2 values (mean ± s.e.m.) relative to Neg-si, which was set as 0 ($n = 3$ independent experiments). Statistical analysis was performed with one-way ANOVA and Tukey's multiple comparison test. NS, not significant; $^{*}P < 0.05$, $^{***}P < 0.001$; error bars indicate s.e.m.

Surprisingly, neither alignment nor EC area was affected by loss of *Eng* (Fig. 8a–c). However, when we analysed EC areas within the aorta of postnatal day 9 mice, we consistently measured an increase in EC areas of about 10% after 4 days of *Eng* deletion (Fig. 8d,e). Together, these findings suggest that mammalian ECs also require *Eng* function for restricting EC sizes. They furthermore indicate that exposing ECs

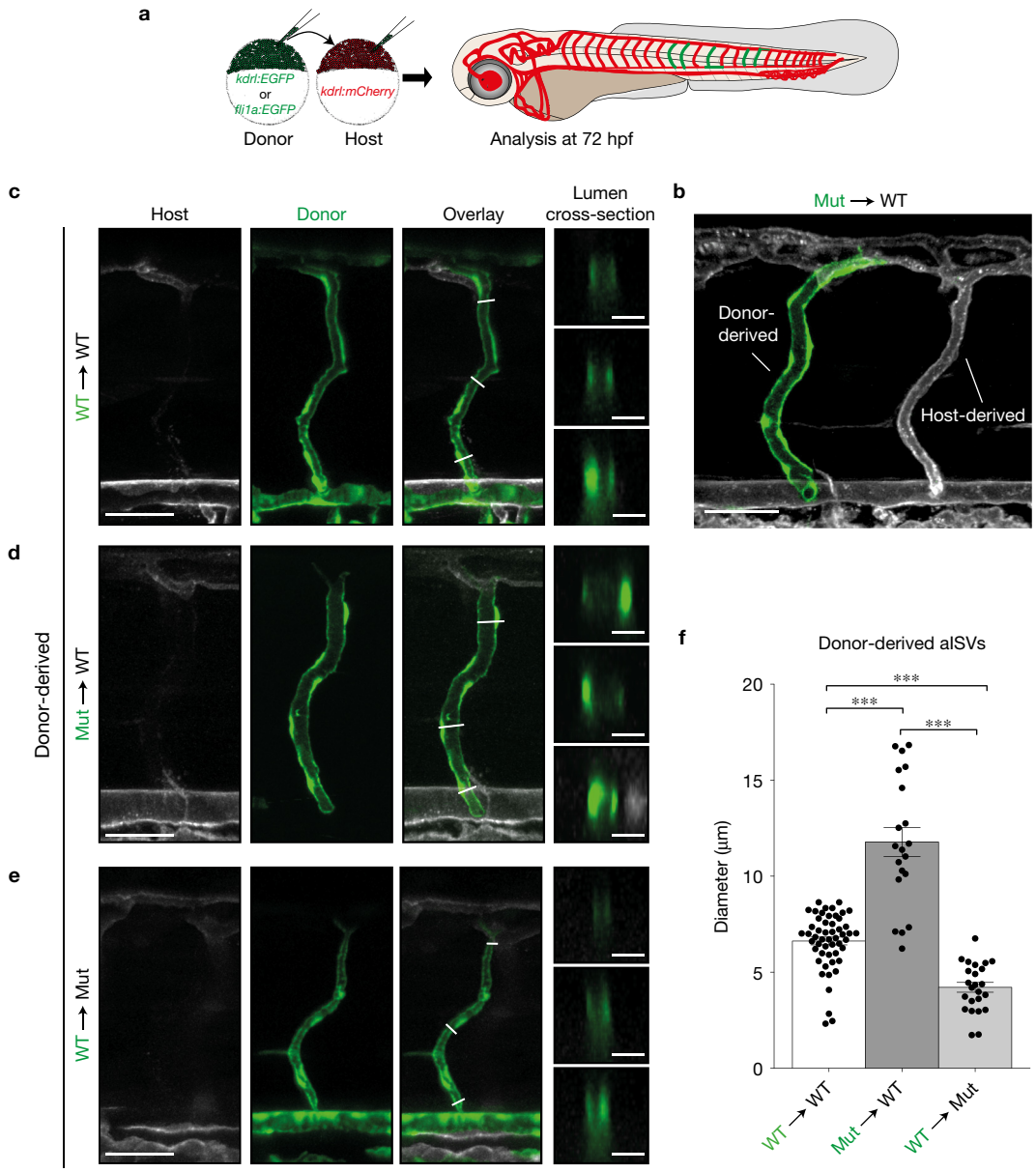

Figure 6 Loss of *eng* function leads to blood vessel enlargement in an EC autonomous manner. (**a**) A schematic of the transplantation scheme, using GFP-labelled donor cells and mCherry-labelled host cells. Analysis of vasculature was performed at 72 hpf. (**b**) Maximum intensity projection of a confocal *z*-stack of a mosaic embryo. Some ISVs can be derived completely from donor cells (note dilation of mutant aISV on the left compared with WT aISV on the right). Scale bar, 50 μm. (**c**–**e**) Representative examples of donor-derived ISVs from WT → WT (**c**) Mut → WT (**d**) and WT → Mut (**e**) transplantations. Optical sections of the lumen reveal complete enclosure by donor cells. Scale bars, 50 μm (overview) and 10 μm (lumen cross-section). (**f**) Quantification of the diameter of donor-derived aISVs (WT → WT $n=52$ vessel segments from 13 ISVs; Mut → WT $n=20$ vessel segments from 5 ISVs; WT → Mut $n=24$ vessel segments from 6 ISVs). Analysed by one-way ANOVA. $^{***}P<0.001$; error bars indicate s.e.m.

to shear stress alone in a culture setting might not influence EC sizes in the same way as a combination of stretch, shear and pressure on matrix-adhered ECs in a tube *in vivo* does.

Our results lead to a model in which two distinct EC responses to a rise in blood flow control proper blood vessel geometries (Supplementary Fig. 7). Initially, EC areas increase, leading to an expansion of vessel diameters. Subsequently, however, ECs react to the increased flow by limiting area expansion and changing their shapes. They elongate and align in the direction of flow. This, in turn, leads to a decrease in blood vessel diameter, while at the same time allowing for the distribution of blood flow to smaller calibre peripheral vessels. In *eng*-deficient vessels, ECs are unable to limit their surface areas. This impedes their alignment in response to flow and dilates the affected vessel, ultimately exacerbating a pre-existing arteriovenous shunt that severely impairs blood flow to surrounding tissues.

Discussion

The assignment of proper calibres to conduits forming tubular networks is instrumental for their correct functioning, and several human disease conditions such as polycystic kidney disease[41] or

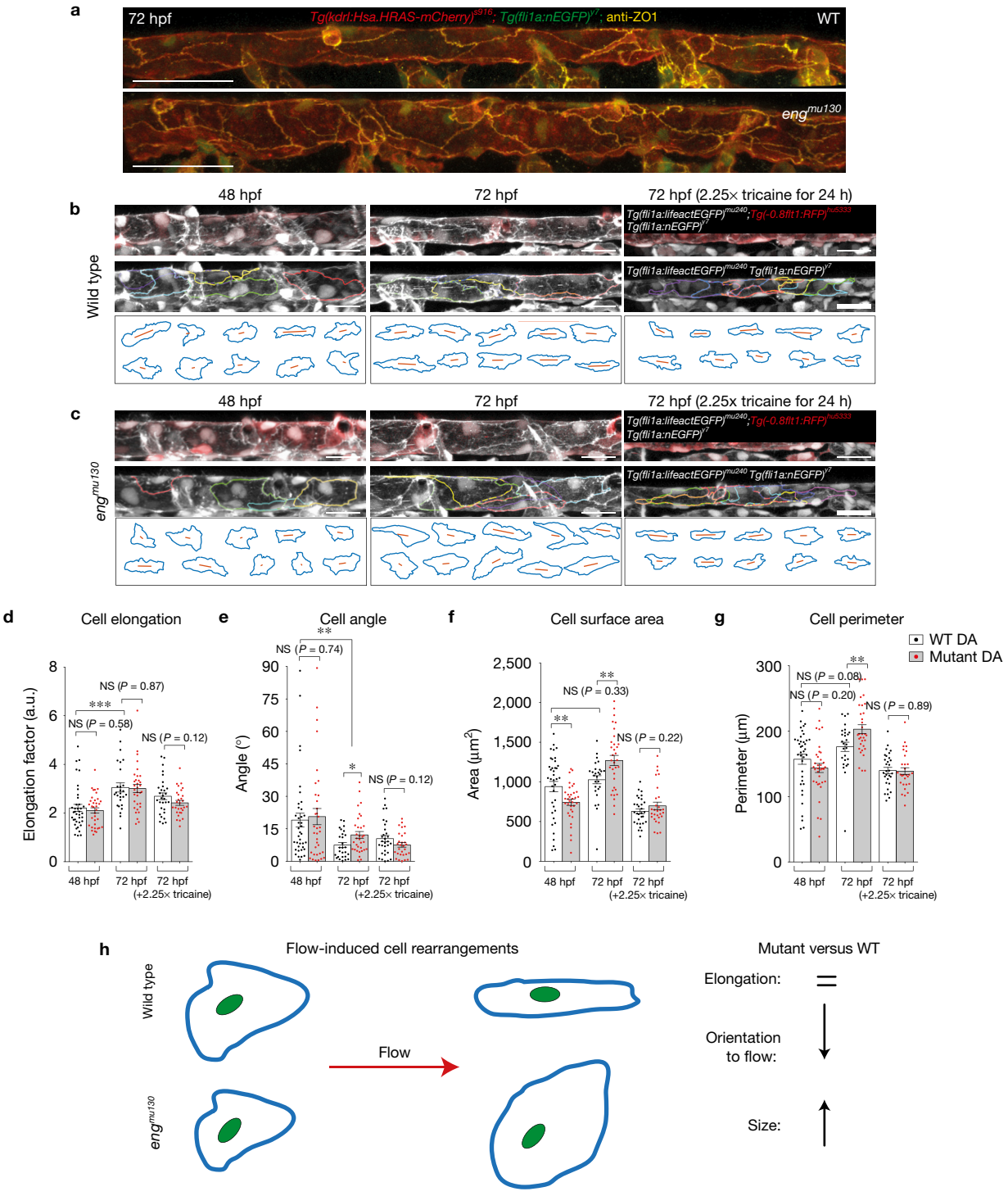

Figure 7 Endoglin function is necessary for blood-flow-induced cell shape changes. (**a**) Maximum intensity projection of a confocal *z*-stack of the DA at 72 hpf. ZO-1 labels EC tight junctions, which are present in both WT and *eng*^{mu130} mutants. Note the relatively disordered arrangement of mutant ECs compared with WT. Representative of 5 WTs and 5 muts. Scale bars, 50 µm. (**b**,**c**) Maximum intensity projection of a confocal *z*-stack of the DA at 48 hpf and 72 hpf (with or without 2.25× tricaine treatment) in WT and *eng*^{mu130} mutants. *Tg(fli1a:lifeactEGFP)*^{mu240} enrichment at cell–cell contacts, together with mosaic *Tg(-0.8flt1:RFP)*^{hu5333} and *Tg(fli1a:nEGFP)*^{y7}, can be used to outline three-dimensional perimeters of cells. Note elongation and alignment of cells at 72 hpf compared with 48 hpf in WTs. *eng*^{mu130} mutant cells have a larger surface area at 72 hpf, but tricaine treatment reduces surface area in both WTs and mutants. Scale bars, 25 µm. (**d**–**g**) Quantification of DA endothelial cell shape parameters: cell elongation, angle, surface area and perimeter in WTs and *eng*^{mu130} mutants (48 hpf: $n = 38$ cells from 2 WTs, $n = 35$ cells from 2 muts; 72 hpf: $n = 27$ cells from 2 WTs, $n = 33$ cells from 2 muts; 72 hpf (2.25× tricaine): $n = 30$ cells from 2 WTs, $n = 29$ cells from 2 muts). Individual fish from 2 independent experiments per condition. See Methods for description of statistical analysis. (**h**) A schematic of flow-induced EC shape changes. Flow causes WT cells to elongate and align without a change in their surface areas. In *eng*^{mu130} mutants, elongation occurs normally, but EC sizes increase considerably. NS, not significant; $^{*}P < 0.05$, $^{**}P < 0.01$, $^{***}P < 0.001$; error bars indicate s.e.m.

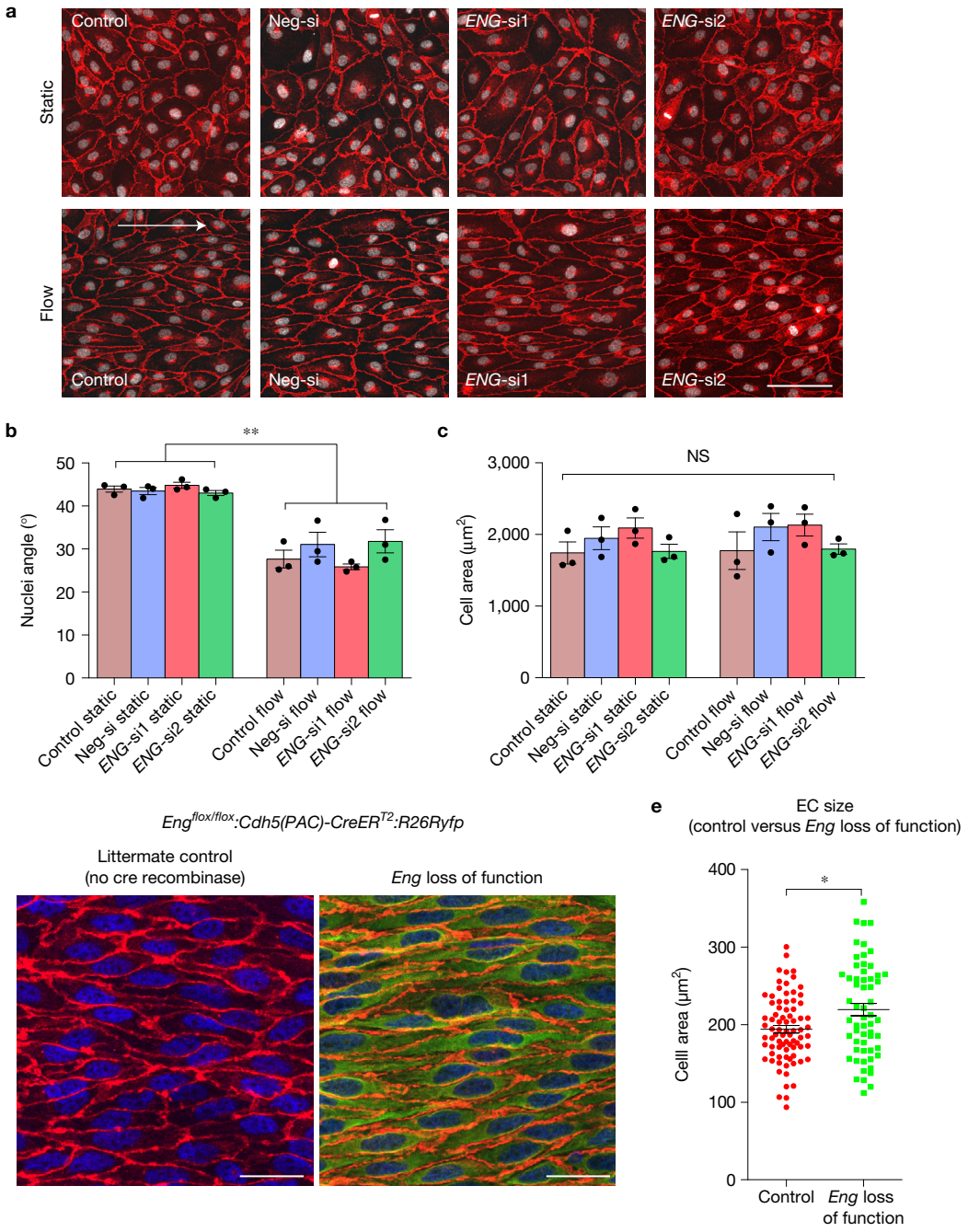

Figure 8 Role of endoglin in controlling the morphology of mammalian ECs exposed to flow. (**a**) VE-cadherin (red) and nuclei (white) staining of HUVEC transfected with siRNAs against ENG or negative siRNA and exposed to unidirectional shear stress of 15 dyn cm^{-2} for 24 h. The arrow represents the flow direction. Scale bar, 100 μm. (**b**) Quantification of the angle of nuclei to the direction of flow (set as 0°) in **a**. The bars represent the mean nuclei angle ($n=3$ independent experiments). (**c**) Cell area, measured by dividing total image area by the number of nuclei. For all quantifications, an average was taken from five random images per sample ($n=3$ independent samples). Statistical analysis was performed with one-way ANOVA and Tukey's multiple comparison test. (**d**) Immunostaining of ECs in thoracic aorta from WT and *Eng*$^{flox/flox}$*:Cdh5(PAC)-CreER*^{T2}*:R26Ryfp* mice at P9 after 50 μg tamoxifen injection at P4. GFP indicates recombination. EC outlines can be distinguished by CD31 labelling (red), and nuclei with ERG (blue). Scale bars, 20 μm. (**e**) Quantification of surface area in ECs of the thoracic aorta in WT and *Eng* loss of function mice (WT aorta: $n=79$ cells from 3 mice; *Eng* KO cells from fully recombined aorta: $n=59$ cells from 3 mice). Analysed by unpaired Student's *t*-test. NS, not significant; $^{*}P<0.05$, $^{**}P<0.01$; error bars indicate s.e.m.

HHT[42] are caused by aberrantly sized tubular organs. While we have great insights into the processes governing the formation of a lumen *per se*[43], the factors controlling different tube sizes are much less understood. Changes in tube diameters can be achieved either via an increase in the numbers of the cells forming the tube, or by changes in cell shapes[44–47]. While haemodynamics can influence both cellular properties[40,48], previous studies showed increased EC numbers within HHT-associated AVMs[16–19]. However, while we detected some

enlarged blood vessels with supernumerary ECs, we also found enlarged blood vessel segments that did not contain more endothelial cells. In these cases, we found that changes in cell shapes caused blood vessel enlargement. Thus, our studies support an additional process, namely restricting EC sizes in response to blood flow, by which *eng* function determines optimal tube diameters. Possible mechanisms might involve integrin signalling, which can influence cell contractility and shape[49,50]. Tzima *et al.* showed that integrin signalling was necessary for EC alignment to flow[51], while a recent study provided evidence that human pathogenic bacteria trigger *eng* expression, thereby activating integrins[52].

Previous studies investigating the influence of haemodynamics on vessel sizes artificially changed blood flow in established vascular networks[5–9,53,54]. Earlier studies showed that arteries are formed by vein-derived cells[25]. Work from the Jakobsson group now provides evidence that *Eng* promotes this redistribution of ECs through facilitating EC migration against the direction of blood flow[55]. Of note, we observed higher EC numbers specifically in enlarged veins in zebrafish *eng* mutants during fin regeneration. Thus, in addition to changes in cell shapes, aberrant cell migration might also contribute to AVM development in zebrafish, as was previously shown to be the case for *alk1* mutants[18].

Thoma already noted that the theory of a shear stress set point is complicated by the shunt problem[13]. Our results now provide a possible solution to this problem. The biphasic EC response to blood flow governed by changes in endothelial cell shapes potently counteracts size increases within blood vessels. Our observations suggest that flow rates change dynamically within the forming embryonic vascular system due to the addition of new blood vessel connections, probably creating arteriovenous shunts that need to be corrected. Endothelial cell shape changes might provide a means to adopt tube sizes within quickly changing haemodynamic environments.

At later stages of embryonic development, blood vessels are invested with contractile smooth muscle cells that control vascular tone. Our results show that haemodynamics affect embryonic blood vessel diameters via a direct influence on EC shapes before smooth muscle cell differentiation[56]. Importantly, previous studies associated changes in smooth muscle cell coverage with AVM formation[22,57]. Therefore, how these two systems of blood vessel size control interact will be of great future interest. Since many tubular organs transport fluid, our results might furthermore describe a general phenomenon how cells lining tubular networks respond to biophysical cues, thereby determining optimal tube diameters. □

METHODS

Methods, including statements of data availability and any associated accession codes and references, are available in the online version of this paper.

Note: Supplementary Information is available in the online version of the paper

ACKNOWLEDGEMENTS

This work was funded by the Max Planck Society (A.F.S.), the Deutsche Forschungsgemeinschaft (DFG SI-1374/3-2; DFG SI-1374/4-1; DFG SI-1374/5-1; A.F.S.), and a European Research Council (ERC) starting grant (260794-ZebrafishAngio; A.F.S.). This work was supported by the Deutsche Forschungsgemeinschaft (DFG) Cells-in-Motion Cluster of Excellence (EXC 1003-CIM), University of Münster, Germany. J.B. was supported by a long-term EMBO post-doctoral fellowship. L.J. was supported by The Swedish Research Council, The Swedish Cancer Society and Karolinska Institutet. We thank H. Arthur for providing the *Eng*$^{flox/flox}$ mice and R. Adams for the *Cdh5(PAC)-CreER*^{T2} mice.

AUTHOR CONTRIBUTIONS

W.W.S. and A.F.S. designed and interpreted the experiments and wrote the manuscript. J.B. identified the zebrafish *eng* homologue and generated the *Tg(klf2a:YFP)*^{mu107} zebrafish. R.T. performed cell culture experiments. E.V.L. performed FACS sorting of zebrafish embryos and performed qPCR experiments. R.M. and C.D. performed particle velocimetry, the optical rail experiments and determined flow parameters. T.A.-W. performed zebrafish cell shape analysis. M.J.H. and W.H. generated *Tg(fli1a:lifeactEGFP)*^{mu240} zebrafish. Y.J. and L.J. determined cell shape changes in *eng* mutant mice.

COMPETING FINANCIAL INTERESTS

The authors declare no competing financial interests.

Published online at http://dx.doi.org/10.1038/ncb3528

1. Ochoa-Espinosa, A. & Affolter, M. Branching morphogenesis: from cells to organs and back. *Cold Spring Harb. Perspect. Biol.* **4,** a008243 (2012).
2. Filosa, J. A., Morrison, H. W., Iddings, J. A., Du, W. & Kim, K. J. Beyond neurovascular coupling, role of astrocytes in the regulation of vascular tone. *Neuroscience* **323,** 96–109 (2016).
3. Joyner, M. J. & Casey, D. P. Regulation of increased blood flow (hyperemia) to muscles during exercise: a hierarchy of competing physiological needs. *Physiol. Rev.* **95,** 549–601 (2015).
4. Baeyens, N. & Schwartz, M. A. Biomechanics of vascular mechanosensation and remodeling. *Mol. Biol. Cell* **27,** 7–11 (2016).
5. Kamiya, A. & Togawa, T. Adaptive regulation of wall shear stress to flow change in the canine carotid artery. *Am. J. Physiol.* **239,** H14–H21 (1980).
6. Langille, B. L. Arterial remodeling: relation to hemodynamics. *Can. J. Physiol. Pharmacol.* **74,** 834–841 (1996).
7. Langille, B. L., Bendeck, M. P. & Keeley, F. W. Adaptations of carotid arteries of young and mature rabbits to reduced carotid blood flow. *Am. J. Physiol.* **256,** H931–H939 (1989).
8. Langille, B. L. & O'Donnell, F. Reductions in arterial diameter produced by chronic decreases in blood flow are endothelium-dependent. *Science* **231,** 405–407 (1986).
9. Tuttle, J. L. *et al.* Shear level influences resistance artery remodeling: wall dimensions, cell density, and eNOS expression. *Am. J. Physiol.* **281,** H1380–H1389 (2001).
10. Baeyens, N. *et al.* Vascular remodeling is governed by a VEGFR3-dependent fluid shear stress set point. *eLife* **4,** e04645 (2015).
11. Kamiya, A., Bukhari, R. & Togawa, T. Adaptive regulation of wall shear stress optimizing vascular tree function. *Bull. Math. Biol.* **46,** 127–137 (1984).
12. Rodbard, S. Vascular caliber. *Cardiology* **60,** 4–49 (1975).
13. Thoma, R. *Untersuchungen über die Histogenese und Histomechanik des Gefässsystems* (Verlag von Ferdinand Enke, 1893).
14. Pries, A. R., Hopfner, M., le Noble, F., Dewhirst, M. W. & Secomb, T. W. The shunt problem: control of functional shunting in normal and tumour vasculature. *Nat. Rev. Cancer* **10,** 587–593 (2010).
15. Tual-Chalot, S., Oh, S. P. & Arthur, H. M. Mouse models of hereditary hemorrhagic telangiectasia: recent advances and future challenges. *Front. Genet.* **6,** 25 (2015).
16. Roman, B. L. *et al.* Disruption of acvrl1 increases endothelial cell number in zebrafish cranial vessels. *Development* **129,** 3009–3019 (2002).
17. Mahmoud, M. *et al.* Pathogenesis of arteriovenous malformations in the absence of endoglin. *Circ. Res.* **106,** 1425–1433 (2010).
18. Rochon, E. R., Menon, P. G. & Roman, B. L. Alk1 controls arterial endothelial cell migration in lumenized vessels. *Development* **143,** 2593–2602 (2016).
19. Tual-Chalot, S. *et al.* Endothelial depletion of Acvrl1 in mice leads to arteriovenous malformations associated with reduced endoglin expression. *PLoS ONE* **9,** e98646 (2014).
20. Kamaid, A. *et al.* Betaglycan knock-down causes embryonic angiogenesis defects in zebrafish. *Genesis* **53,** 583–603 (2015).
21. Lee, N. Y. *et al.* Endoglin regulates PI3-kinase/Akt trafficking and signaling to alter endothelial capillary stability during angiogenesis. *Mol. Biol. Cell* **23,** 2412–2423 (2012).
22. Li, D. Y. *et al.* Defective angiogenesis in mice lacking endoglin. *Science* **284,** 1534–1537 (1999).
23. Gougos, A. & Letarte, M. Primary structure of endoglin, an RGD-containing glycoprotein of human endothelial cells. *J. Biol. Chem.* **265,** 8361–8364 (1990).
24. Seghers, L. *et al.* Shear induced collateral artery growth modulated by endoglin but not by ALK1. *J. Cell Mol. Med.* **16,** 2440–2450 (2012).
25. Xu, C. *et al.* Arteries are formed by vein-derived endothelial tip cells. *Nat. Commun.* **5,** 5758 (2014).
26. Childs, S., Chen, J. N., Garrity, D. M. & Fishman, M. C. Patterning of angiogenesis in the zebrafish embryo. *Development* **129,** 973–982 (2002).
27. Chen, Q. *et al.* Haemodynamics-driven developmental pruning of brain vasculature in zebrafish. *PLoS Biol.* **10,** e1001374 (2012).

28. Kochhan, E. *et al.* Blood flow changes coincide with cellular rearrangements during blood vessel pruning in zebrafish embryos. *PLoS ONE* **8,** e75060 (2013).
29. Atri, D., Larrivee, B., Eichmann, A. & Simons, M. Endothelial signaling and the molecular basis of arteriovenous malformation. *Cell Mol. Life Sci.* **71,** 867–883 (2014).
30. Bagatto, B. & Burggren, W. A three-dimensional functional assessment of heart and vessel development in the larva of the zebrafish (Danio rerio). *Physiol. Biochem. Zool.* **79,** 194–201 (2006).
31. Malone, M. H. *et al.* Laser-scanning velocimetry: a confocal microscopy method for quantitative measurement of cardiovascular performance in zebrafish embryos and larvae. *BMC Biotechnol.* **7,** 40 (2007).
32. Jamison, R. A., Samarage, C. R., Bryson-Richardson, R. J. & Fouras, A. *In vivo* wall shear measurements within the developing zebrafish heart. *PLoS ONE* **8,** e75722 (2013).
33. Pappano, A. J. & Wier, W. G. *Cardiovascular Physiology* (Elsevier/Mosby, 2013).
34. Zhong, M. C., Wei, X. B., Zhou, J. H., Wang, Z. Q. & Li, Y. M. Trapping red blood cells in living animals using optical tweezers. *Nat. Commun.* **4,** 1768 (2013).
35. Levesque, M. J. & Nerem, R. M. The elongation and orientation of cultured endothelial cells in response to shear stress. *J. Biomech. Eng.* **107,** 341–347 (1985).
36. Boon, R. A. *et al.* KLF2-induced actin shear fibers control both alignment to flow and JNK signaling in vascular endothelium. *Blood* **115,** 2533–2542 (2010).
37. Nicoli, S. *et al.* MicroRNA-mediated integration of haemodynamics and Vegf signalling during angiogenesis. *Nature* **464,** 1196–1200 (2010).
38. Melchionna, R. *et al.* Laminar shear stress inhibits CXCR4 expression on endothelial cells: functional consequences for atherogenesis. *FASEB J.* **19,** 629–631 (2005).
39. Hultin, S. *et al.* AmotL2 links VE-cadherin to contractile actin fibres necessary for aortic lumen expansion. *Nat. Commun.* **5,** 3743 (2014).
40. Corti, P. *et al.* Interaction between alk1 and blood flow in the development of arteriovenous malformations. *Development* **138,** 1573–1582 (2011).
41. Ong, A. C., Devuyst, O., Knebelmann, B. & Walz, G. Autosomal dominant polycystic kidney disease: the changing face of clinical management. *Lancet* **385,** 1993–2002 (2015).
42. McDonald, J., Bayrak-Toydemir, P. & Pyeritz, R. E. Hereditary hemorrhagic telangiectasia: an overview of diagnosis, management, and pathogenesis. *Genet. Med.* **13,** 607–616 (2011).
43. Sigurbjornsdottir, S., Mathew, R. & Leptin, M. Molecular mechanisms of *de novo* lumen formation. *Nat. Rev. Mol. Cell Biol.* **15,** 665–676 (2014).
44. Costantini, F. & Kopan, R. Patterning a complex organ: branching morphogenesis and nephron segmentation in kidney development. *Dev. Cell* **18,** 698–712 (2010).
45. Forster, D. & Luschnig, S. Src42A-dependent polarized cell shape changes mediate epithelial tube elongation in *Drosophila*. *Nat. Cell Biol.* **14,** 526–534 (2012).
46. Lubarsky, B. & Krasnow, M. A. Tube morphogenesis: making and shaping biological tubes. *Cell* **112,** 19–28 (2003).
47. Zuo, L., Iordanou, E., Chandran, R. R. & Jiang, L. Novel mechanisms of tube-size regulation revealed by the *Drosophila* trachea. *Cell Tissue Res.* **354,** 343–354 (2013).
48. Dietrich, A. C., Lombardo, V. A., Veerkamp, J., Priller, F. & Abdelilah-Seyfried, S. Blood flow and Bmp signaling control endocardial chamber morphogenesis. *Dev. Cell* **30,** 367–377 (2014).
49. Kim, C., Ye, F. & Ginsberg, M. H. Regulation of integrin activation. *Annu. Rev. Cell Dev. Biol.* **27,** 321–345 (2011).
50. Munjal, A. & Lecuit, T. Actomyosin networks and tissue morphogenesis. *Development* **141,** 1789–1793 (2014).
51. Tzima, E., del Pozo, M. A., Shattil, S. J., Chien, S. & Schwartz, M. A. Activation of integrins in endothelial cells by fluid shear stress mediates Rho-dependent cytoskeletal alignment. *EMBO J.* **20,** 4639–4647 (2001).
52. Muenzner, P., Bachmann, V., Zimmermann, W., Hentschel, J. & Hauck, C. R. Human-restricted bacterial pathogens block shedding of epithelial cells by stimulating integrin activation. *Science* **329,** 1197–1201 (2010).
53. Tulis, D. A., Unthank, J. L. & Prewitt, R. L. Flow-induced arterial remodeling in rat mesenteric vasculature. *Am. J. Physiol.* **274,** H874–H882 (1998).
54. Unthank, J. L., Nixon, J. C., Burkhart, H. M., Fath, S. W. & Dalsing, M. C. Early collateral and microvascular adaptations to intestinal artery occlusion in rat. *Am. J. Physiol.* **271,** H914–H923 (1996).
55. Jin, Y. *et al.* Endoglin prevents vascular malformation by regulating flow-induced cell migration and specification through VEGFR2 signalling. *Nat. Cell Biol.* http://dx.doi.org/10.1038/ncb3534 (2017).
56. Whitesell, T. R. *et al.* An α-smooth muscle actin (acta2/αsma) zebrafish transgenic line marking vascular mural cells and visceral smooth muscle cells. *PLoS ONE* **9,** e90590 (2014).
57. Mancini, M. L. *et al.* Endoglin plays distinct roles in vascular smooth muscle cell recruitment and regulation of arteriovenous identity during angiogenesis. *Dev. Dyn.* **238,** 2479–2493 (2009).

DOI: 10.1038/ncb3528

METHODS

Zebrafish strains. Zebrafish were maintained as described previously[58]. Transgenic lines and mutants used were *Tg(kdrl:EGFP)*^{s843}, *Tg(kdrl:Hsa.HRAS-mCherry)*^{s916}, *Tg(fli1a:nEGFP)*^{y7}, *Tg(fli1a:EGFP)*^{y1}, *Tg(dll4:gal4*^{FF}*)*^{mu106}, *Tg(UAS:GFP)*^{nkuasgfp1a}, Tg*(-0.8flt1:RFP)*^{hu5333}, *Tg(gata1a:DsRed)*^{sd2}, *Tg(fli1a:lifeactGFP)*^{mu240}, Casper *(mitfa*$^{w2/w2}$*; roy*$^{a9/a9}$*)*. References for all zebrafish lines can be obtained on http://zfin.org. Zebrafish used in this study were between 1 and 2 years of age and were not selected for gender. All animal experiments were performed in compliance with the relevant laws and institutional guidelines and were approved by local animal ethics committees of the Landesamt für Natur, Umwelt und Verbraucherschutz Nordrhein-Westfalen.

Mice. *Eng*$^{flox/flox}$*:Cdh5(PAC)CreER*^{T2}*:R26Ryfp* were generated by inter-crosses of the following mice: *Eng*$^{flox/flox}$ (ref. 59), *Cdh5(PAC)-CreER*^{T2} (ref. 60), and R26Ryfp (also denoted Ai3 in short or alternatively B6.Cg-*Gt(ROSA)26Sor*$^{tm3(CAG-EYFP)Hze}$/J (Stock Number 007903, The Jackson Laboratory). Animal housing and procedures were in accordance with Swedish legislation and approved by the local animal ethics committees.

Identification of zebrafish *endoglin* homologue. Identification of Eng and Tgfbr3 orthologues in zebrafish was performed on the basis of homology searches to the most conserved C-terminal cytoplasmic domain, encoded in the two last coding exons of the respective human genes. Synteny was identified on the basis of Ensembl. The following proteins were identified:
Mus musculus (mouse) Eng: ENSMUSP00000009705
Mus musculus Tgfbr3: ENSMUSP00000031224
Monodelphis domestica (opossum) Eng: ENSMODP00000006956
Taeniopygia guttata (zebra finch) Eng: ENSTGUP00000003672
Taeniopygia guttata Tgfbr3: ENSTGUP00000006307
Homo sapiens (human) Eng: ENSP00000341917
Homo sapiens Tgfbr3: ENSP00000212355
Gallus gallus Tgfbr3: ENSGALP00000032713
Anolis carolinensis Tgfbr3: ENSACAP00000001391
Xenopus tropicalis Tgfbr3: ENSXETP00000049788
Danio rerio (zebrafish) Tgfbr3: ENSDARP00000133083
Gasterosteus aculeatus (stickleback) Eng: ENSGACP00000021916
Gasterosteus aculeatus Tgfbr3: ENSGACP00000005710
Takifugu rubripes (fugu) Tgfbr3: ENSTRUP00000032677
Oryzias latipes (medaka) Eng: ENSORLP00000008428
Oryzias latipes Tgfbr3: ENSORLP00000017470

In addition, genomic sequence encoding syntenic homologous sequences were identified for:
Xenopus tropicalis Eng: JGI4.2: GL172790.1:2077326-2079133
Fugu rubripes Eng: FUGU 4.0 scaffold_44:587239-594140
Danio rerio Eng: GRCz10: Chromosome 5:70875139-70877042

The respective protein sequences were predicted using GenomeScan with the C terminus of human ENG as a template. Phylogenetic analysis was performed using MEGA7. Multiple sequence alignment was performed using ClustalW, and a phylogenetic tree was generated using the neighbour-joining method.

Generation of zebrafish *eng* mutants. *eng* mutants were generated by TALEN mutagenesis. TALENs specific to *eng* were designed using the online TAL Effector Nucleotide Targeter (https://tale-nt.cac.cornell.edu) with the first exon provided as the target sequence. Criteria for optimal TALEN pairs were followed as described[61]. The following TALEN pair was selected for optimal length and presence of an MspI site in the spacer, facilitating identification of mutations by PCR and digest.
5′ TALEN arm
DNA sequence: 5′-tgctgtgtttgcttct-3′
RVD sequence: NN HD NG NN NG NN NG NG NG NN NI HD NG NG HD NG
3′ TALEN arm
DNA sequence: 5′-tggagctcttacctga-3′
RVD sequence: NN NN NI NN HD NG HD NG NG NI HD HD NG NN NI
RVDs were assembled using the Golden Gate TALEN kit v2.0 (Addgene), into pTAL4 vectors.

Genotyping. To detect TALEN activity and later identify genomic lesions, primers End_TAL6 FWD (5′-tcttgcagccctaatcagc-3′) and End_TAL6 REV (5′-agcaactgta aaattaccacaaca-3′) were used to amplify a 418 bp fragment spanning the TALEN-binding site and spacer region. After MspI digestion, WT amplicons cleave to 246 bp + 172 bp fragments. DNA amplified from the *eng*^{mu130} allele does not digest.

Generation of transgenic lines. The *Tg(fli1a:eng-GFP)*^{mu156} construct was generated via Gateway cloning (Invitrogen). Primers Eng attB1 (5′GGGGACAAGTTTG TACAAAAAAGCAGGCTccaccatgaagagcatctgctgtgtttt-3′) and Eng NOS attB2 (5′-GGGGACCACTTTGTACAAGAAAGCTGGGTatgccatgctgctggtgggtg-3′) were used to amplify the full-length zebrafish endoglin ORF from an EST obtained from Open Biosystems (EDR4422-98253197). This fragment was cloned into the Gateway entry vector pDONR221 via standard BP reaction to generate Dr eng NO STOP pDONR221. For vascular-specific expression and visualization of protein localization, we performed LR reaction with Dr eng NO STOP pDONR221, p5EntryFli1ep and p3Eegfp into the pDestTol2aspA destination vector[62]. Plasmid DNA was isolated by Midiprep (Qiagen) and injected into *eng*^{mu130} homozygous mutant embryos at ∼25 pg per embryo together with ∼50 pg *tol2* transposase mRNA[63].

To generate the Tg*(klf2a:YFP)*^{mu107} line, BAC recombineering was employed as previously described[63]. BAC clone CH73-180A21 (obtained from Children's Hospital Oakland Research Institute) containing the entire *klf2a* gene was modified by addition of iTol2 sites and insertion of a Citrine cassette at the ATG of *klf2a*.
klf2a:YFP intensity measurements.

Embryos were crossed in such a way as to ensure that only one copy of *Tg(kdrl:Hsa.HRAS-mCherry)*^{s916} and *Tg(klf2a:YFP)*^{mu107} were present. Experiments were performed three times and imaged on the same microscope with the same settings for the same time points (but not between time points). Imaris was used to crop away epidermis and the far side of the embryo as much as possible. ImageJ was used to calculate average pixel intensities on maximum intensity projections using the mCherry channel to outline vessels of interest.

Immunohistochemistry and whole-mount *in situ* hybridization. The *klf2a* probe was described previously[37]. The *endoglin* ISH probe was generated from the aforementioned EST from Open Biosystems (EDR4422-98253197). In brief, the plasmid was linearized with SalI and IVT reaction performed with Sp6 polymerase for antisense probe synthesis. Whole-mount *in situ* hybridization of zebrafish embryos was performed as described previously[37]. For visualization of tight junctions, we performed immunostaining with mouse monoclonal anti-human ZO-1 antibody (Invitrogen 339100). Embryos were fixed in 2% PFA/PBSTween (0.3%) overnight at 4 °C. Embryos were washed 4 × 5 min in PBSTween (0.3%), and then permeabilized in 100% acetone for 5 min at −20 °C. Embryos were then given 2 quick washes, followed by 3 × 5 min and 1 × 15 min in PBSTx (0.3% Tween20, 0.6% TritonX-100.). They were further permeabilized for 5 min with 10 µg µl^{-1} Proteinase-K in PBSTx (0.3% Tween 20, 0.6% TritonX-100). Digestion was stopped with 4% PFA for 20 min at room temperature. Embryos were blocked for 2 h in blocking solution (0.6% TritonX-100, 10% normal goat serum, 1% BSA, 0.01% sodium azide in PBSTween (0.3%)). Primary antibody was diluted 1:200 in blocking solution on a 4 °C shaker overnight. The following day, embryos were washed 6 × 1 h in PBSTween (0.3%). Embryos were incubated in AlexaFluor goat anti-mouse 546 secondary antibody (Invitrogen A11003) diluted 1:1,000 in PBSTween (0.3%) overnight on a 4 °C shaker. Embryos were washed at least 6 × 1 h in PBSTween (0.3%) prior to imaging. All experiments were performed at least three times (with the exception of the *eng* ISH in *eng*^{mu132} embryos, which was performed two times).

eng nonsense-mediated decay. Stainings were performed on embryos obtained from heterozygous incrosses. All WT and *eng*^{mu132} embryos had a characteristic 'dark' staining pattern, while embryos from *eng*^{mu130} + /− incrosses had clearly 'dark,' 'medium' and 'light' staining patterns. All embryos were imaged and genotyped.

'*n*/*n*' reports the 'number of embryos with staining pattern in image'/'total embryos from 3 experiments'.

In *eng*^{mu130} + /− incross embryos, +/+, +/− and −/− genotypes invariably correlated with 'dark,' 'medium' and 'light' staining patterns.

klf2a in situ hybridization. Stainings were done on embryos obtained from heterozygous incrosses. Embryos were pre-sorted on the basis of 'light' staining in axial vessels in trunk or 'dark' staining particularly in PCV, and then genotyped.

'*n*/*n*' reports the 'number of embryos with indicated genotype'/'total no. of embryos of that genotype in 3 experiments that had pre-sorted staining pattern as in picture'.

WTs and heterozygous embryos were indistinguishable with 'light' trunk expression, while most *eng*^{mu130} mutants had clearly enhanced staining in PCV.

Live imaging and microscopy. Embryos were mounted in 1% low-melting-point agarose in E3 medium supplemented with 168 mg l^{-1} tricaine (1×) and 0.003% phenylthiourea (to prevent pigment formation) for all live imaging experiments. Confocal *z*-stacks were acquired on inverted SP5 (Leica Microsystems) and LSM780 (Zeiss) scanning confocal microscopes. For 24 h time lapses and blood flow measurements, stage incubation was used to maintain constant temperature of 28.5 °C.

Morpholino injections, microangiography and drug treatments. Morpholinos were obtained from Gene Tools, resuspended in distilled H_2O and around

2 nl injected into 1-cell-stage embryos to deliver the following doses: standard control MO 5′-CCTCTTACCTCAGTTACAATTTATA-3′ (4 ng per embryo) *tnnt2a* MO 5′-CATGTTTGCTCTGATCTGACACGCA-3′ (4 ng per embryo) Microangiography was performed as described previously[28] using Qdots 633 nm (Life Technologies). For nifedipine treatments, nifedipine (Sigma-Aldrich) was dissolved in dimethylsulfoxide to 10 mM stock concentration, and diluted in E3 medium to 15 μM (together with final concentration 2× tricaine). Embryos were treated from 48 to 52 hpf and fixed in 4% PFA overnight at 4 °C.

Genetic ablation of Eng in mouse aorta. Mice were injected with 50 μg tamoxifen at P4 and euthanized at P9. Both males and females were included in the analysis. Thoracic aortae were excised and fixed in 4% PFA for 2 h at room temperature. Whole-mount staining was performed with antibodies against CD31, GFP and ERG1 and samples were flat mounted and imaged using an SP8 Leica microscope.

Antibodies: goat anti-mouse CD31 (AF3628, R&D Systems 1:500); rabbit anti-ERG (clone: EPR3864, ab92513, Abcam, 1:500); chicken anti-GFP (ab13970, Abcam, 1:1,000);

Secondary antibodies used were: donkey anti-goat IgG Cy3 (705-166-147, JacksonImmunoResearch, 1:400), donkey anti-chicken IgY (IgG) Alexa488 (703-545-155, JacksonImmunoResearch, 1:400), donkey anti-rabbit IgG Alexa647 (A31573, Life Technologies, 1:500).

Blastomere transplantations. Cell transplantations were performed as described previously[64]. All experiments were performed at least 3 times. For aISV diameter calculations, around 6–10 measurements were taken in each of 4 quadrants along the aISV (2 below the horizontal myoseptum and 2 above). From the measurements, averages were taken for each of 3 possible categories (Donor only, Host only, mosaic) in each quadrant. For final tabulation, each ISV contributed data points from each quadrant, with a maximum possibility of 3 values per quadrant (depending on composition). This is important, as we measured a significant increase in diameter of normal WT aISVs as they travel from the DA to dorsal longitudinal anastomotic vessel (DLAV), and therefore the effect of donor cell incorporation must also reflect where in the vessel they reside.

Fin regeneration experiments. Fin amputations were performed as previously described[25].

Morphology of adult brain blood vessels. To characterize morphology of the brain vasculature, adult zebrafish were euthanized and freshly dissected brains were imaged immediately on a stereomicroscope. Images shown in Fig. 1 are representative of results obtained in 5 WTs and 5 mutants from 3 independent experiments.

ISV remodelling. To examine ISVs in juvenile zebrafish, embryos were obtained from incrosses of Casper +/−; *eng*^{mu130}+/− parents. Fish were sorted for the Casper phenotype (lack of pigmentation) and *eng*^{mu130} mutants and siblings (+/+ and +/−) were separated and entered into the fish system. Imaging of the trunk ISVs over the yolk extension was done at 17 days post fertilization (dpf).

Images (×20 magnification) were made of ISVs over the yolk extension in 17 dpf juveniles expressing the *Tg(kdrl:EGFP)*^{s843} and *Tg(gata1a:DsRed)*^{sd2} trangenes. This corresponded to ∼10–12 ISVs per fish. Fish were excluded if they had not developed prominent intercostal vessels by this time, indicative of developmental delay. Analysis was performed on 3 separate clutches. aISVs and vISVs were quantified on the basis of morphology (connection to DA or PCV). A remodelling event was defined as an ISV that no longer made a connection to the DLAV or DA/PCV. RBC perfusion was defined as the presence of a DsRed^{+} erythrocyte in the lumen anywhere along the length of the ISV.

Optical rail. Optical rail experiments in zebrafish were done in 72 hpf zebrafish embryos inside an Okolab tabletop incubator at 28.5 °C. Fish embryos were mounted in WillCo Wells 100-μm-thick glass-bottom dishes. A 1,064 nm 3W cw Cobolt Rumba laser was used for trapping. A Hamamatsu X10468-13 spatial light modulator was used together with Red Tweezers[20] to holographically modulate the beam for rough positioning of the laser beam on the capillary entrance. A CFI P-Apo IR 60× WI/1.27/0.17 objective from Nikon was used to focus the laser into the sample plane of a Nikon Ti-E 2000 microscope. A shutter from Thorlabs was used to block the laser beam before the microscope during 'off' periods of the measurement. The motorized stage of the microscope was used for fine positioning of the sample with regard to the laser. An IDS Germany GmbH uEye337x-CP camera was used for video acquisition during experiments. Videos were taken for 30 s without the laser, 30 s with the laser and 30 s without the laser consecutively. The laser was blocked by the shutter during periods without the laser.

Flow parameter analysis. High-speed videos of zebrafish embryos were acquired of embryos inside the Okolab heating chamber at 28.5 °C. Fish were kept at rest for 5 min inside this chamber prior to video acquisition. Further fish were kept inside an Eppendorf Galaxy 48 S. Fluorescence videos were taken with the IDT NX8-S2 camera at 30 frames per second for 33 s. High-speed bright-field videos were acquired with the same camera at 2,000 frames per second with maximum number of frames possible. Due to the limited memory of the NX8-S2 only 5,000 to 6,000 frames could be acquired leading to a measurement of roughly 10 heartbeat cycles. The region of interest was chosen to acquire both DA and PCV above the yolk extension right before the anal pore. Camera angle was chosen such that the blood flow was going along x or horizontal direction of the videos. Flow videos were analysed with MPIV (Matlab Particle Image Velocimetry)[65] to obtain velocity values of RBCs over time. To improve contrast, a background correction was done by averaging over 50 frames evenly distributed over the whole video and subtracting this averaged frame from the evaluated frames. These frames show only RBCs and no more background. Fluorescence images were meaned along the whole fluorescence video to average over the size of the vessel during dilation and constriction. The image was merged with a normal bright-field frame as a reference of where RBCs were flowing. Vessel walls were then manually outlined. Flow velocity profiles were averaged over 5 consecutive frames to minimize velocity noise. Velocity profiles along the cross-section of the vessel were fitted with a parabolic function. For testing, linear flow profiles were fitted, but quality-of-fit investigations, especially R-squared values, showed a better fit of the parabolic fit as did Jamison *et al.* 2013[32] and in contrast to Hove *et al.* 2003[66]. Due to the size of the region of interest in the video and the quality of the PIV results, 10–14 such cross-sections per fish could be evaluated leading to an equal number of parabolic curves for DA and PCV for each time point obtained. Through these, shear-rate-over-time graphs were calculated and extremal points were averaged over all frames and all positions along the vessels measured to yield one value per fish (Fig. 2f–k). Shear stress was calculated by $\sigma = \eta(\mathrm{d}v/\mathrm{d}y)$, where η is the viscoelasticity of the medium, that is, the blood, and $\mathrm{d}v/\mathrm{d}y$ is the derivative of the parabolic fit along the vessel evaluated at the vessel walls. The viscoelasticity of the medium was assumed to be purely viscous, that is, real in values, and to be 5 times the value of water at the respective temperature according to Anton *et al.* 2013[67]. We have to clarify that an accurate determination of *in vivo* shear rate would include a proper investigation of the viscoelastic nature of the blood *in vivo* and taking into account other effects, such as the Fåhræus–Lindqvist effect[68]. Pulsatility index values were calculated from extremal velocity flow profiles[69]. Values between WT and *eng*^{mu130} fish were compared by Mann–Whitney U test due to unknown distribution of points. Evaluation was performed with custom-written Matlab codes (The MathWorks GmbH).

Capillary red blood cell flow. Presence of RBC flow and direction of flow was scored along every position of the trunk on both sides of the embryo. Data are presented as the percentage of total ISVs scored at every position that had active RBC passage. For images of 30, 48 and 72 hpf embryos with the *Tg(gata1a:DsRed)*^{sd2} transgene, surfaces were used in Imaris to generate masks around the *Tg(kdrl:EGFP)*^{s843} channel to remove DsRed fluorescence from neurons, hypochord and other non-erythrocyte sources.

Flow block experiments. 'n/n' reports the 'number of embryos with staining pattern in image'/'total embryos from 3 experiments'.

Cell culture experiments. HUVEC (Invitrogen) were cultured in M200 medium supplemented with LSGS (Invitrogen) and used until passage 4. The cells were transfected with 20 nM Silencer Select Pre-designed siRNA (Ambion):

ENG-si1 (s4677): 5′-UGACCUGUCUGGUUGCACAtt-3′

ENG-si2 (s4678): 5′-GGACUGUCUUCAUGCGCUUtt-3′

Silencer Select Negative Control no. 1 siRNA using Oligofectamine and used for flow experiments 48 h after transfection. Downregulation was confirmed with qPCR and western blot using anti-ENG antibody (no. 14606, Cell Signaling, dilution 1:1,000) and anti-tubulin antibody (T6199, Sigma, dilution 1:4,000) as loading control. HUVEC were seeded at the density 5×10^4 cells cm^{-2} in μ-Slide$^{0.4}$ Luer (ibidi) and allowed to attach for 3 h. Afterwards the cells were exposed to shear stress of 15 dyn cm^{-2} for 4 h (for qPCR) using the ibidi Pump System. For alignment experiments HUVEC were exposed to shear stress of 15 dyn cm^{-2} for 24 h starting with 5 dyn cm^{-2} and 10 dyn cm^{-2} for 1 h each. Afterwards cells were fixed with 4% PFA and permeabilized with 1% Triton X-100. VE-cadherin was visualized with anti-VE-cadherin antibody (no. 55561, BD, dilution 1:200) together with anti-mouse Alexa Fluor 546 secondary antibody (A11003, Invitrogen, dilution 1:200), and nuclei were stained with Hoechst 33342 (1 μg ml^{-1}). Five random images were taken for quantification with a Leica SP5 microscope at ×20 magnification. Angle of the nuclei to the direction of flow was measured with ImageJ. No cell lines used in this study were found in the database of commonly misidentified cell lines that is maintained by ICLAC and NCBI Biosample. The cell lines were not authenticated. The cell lines were not tested for mycoplasma contamination.

DOI: 10.1038/ncb3528

FACS sorting of ECs from zebrafish embryos. Arterial and venous ECs were obtained from pooled triple-transgenic 72 hpf zebrafish embryos. *Tg(kdrl:Hsa.HRAS-mCherry)*^{s916} exhibits pan-endothelial expression, and the combination of *Tg(dll4:gal4)*^{mu106}; *(UAS:GFP)*^{nkuasgfp1a} labels the arterial ECs within this population. Embryos were deyolked in calcium-free Ringer's solution and treated with 0.5% trypsin–EDTA (Gibco, 15400-054) plus 50 mg ml^{-1} collagenase Type IV (Gibco,17104-019) and dissociated by constant pipetting. The reaction was stopped by adding 5% FBS and the cells were pelleted by centrifuging at 350*g* for 5 min at 4 °C. The pelleted cells were washed twice with 1× HBSS buffer (Gibco, 14185052) and passed through 40 µm nylon filters. Fluorescent-activated cell sorting (FACS) was performed on the cell suspension for arterial (Cherry$^+$/GFP$^+$) and the venous (Cherry$^+$) cells at room temperature. The sorted cells were collected in RLT buffer for RNA isolation.

qPCR experiments. RNA was isolated using the RNeasy Micro Kit (Qiagen) and cDNA was produced with iScript cDNA Synthesis Kit (BioRad). qPCR was performed using Power SYBR Green PCR Master Mix (Applied Biosystems). Relative expression was calculated with qBase software using RPL13A (HUVEC) or *rpl13a* (zebrafish) as endogenous control. Statistical analysis was performed using CNRQ values from qBase.

Human qPCR primers:
ENG-fwd: 5′-TGCTCATGTCCTTGATCCAG-3′
ENG-rev: 5′-CTTCAAATGCGCAACAAGC-3′
KLF2-fwd: 5′-CTTCTCTCCCACCGGGTCTA-3′
KLF2-rev: 5′-TAGCCCAAAAATGCCCACCT-3′
CXCR4-fwd: 5′-GCCCTCCTGCTGACTATTCC-3′
CXCR4-rev: 5′-GGCAGGATAAGGCCAACCAT-3′
RPL13A-fwd: 5′-TCGTACGCTGTGAAGGCATC-3′
RPL13A-rev: 5′-CAGCATACCTCGCACGGTC-3′
Zebrafish qPCR primers:
rpl13a-fwd: 5′-TCTGGAGGACTGTAAGAGGTATGC-3′
rpl13a-rev: 5′-AGACGCACAATCTTGAGAAGCAG-3′
eng-fwd: 5′-GCCGGAGATCCACAGCTTCAGA-3′
eng-rev: 5′-GTTATCGAAAAGCATGGCGTGGC-3′

Blood vessel diameter, cell number and cell shape analysis. For DA and PCV diameter calculations (72 hpf embryos), measurements were taken at the midway point between ISVs along the yolk extension (ISVs no. 5–14), and the mean used as an average diameter per embryo. Similarly, nuclei counts were obtained for the axial vessels over the yolk extension (between ISVs no. 5–14). For ISV diameter, 4 measurements were made along each ISV between the DA and the DLAV and averaged to obtain an average ISV diameter. Nuclei were also counted in each ISV. Reported values come from ISVs no. 5–14 that had RBC flow.

To obtain diameter and nuclei measurements in regenerating fins at 5 dpa, blood flow videos were examined to identify AVMs in *eng*^{mu130} mutants. For each mutant, a WT fin was chosen simultaneously for pairwise analysis on the basis of similar blood flow and vascular outgrowth at the location of the AVM in the mutant. ImageJ was used to trace a 200 µm length of artery beneath the AVM, and ~15–20 equally spaced diameter measurements were used to obtain an average diameter. ECs residing in this 200 µm of vessel were also counted. Diameter and EC number were measured the same way in the vein downstream of the AVM. In the accompanying WT, 200 µm of artery in a similar region and the larger of the two paired veins was analysed in the same way.

For cell shape analysis in zebrafish, images were taken with a 40× water objective of the DA just posterior to the anal pore (small working distance meant this location was easier to image than more anterior over the yolk extension). Two WT and two mutant fish with similar total DA cell numbers were selected and cell shapes were analysed as described above. For analysis of EC size in mouse aorta preparations, the outlines of the aortic ECs were identified by CD31 staining. The area of each EC was measured in Volocity.

To analyse cell shapes in zebrafish embryos, apical cell outlines were traced manually using Imaris. About 100 measurement points were generated per cell on average. These points were then unrolled onto a two-dimensional surface as follows. First, an axis was fitted through the centre of the blood vessel in such a way that the measurement points lie as close to one curve as possible, when projected on a surface perpendicular to the axis. This was done by varying orientation and position of the axis and minimizing the variation in distance from the axis to measurement points that were grouped according to angle with respect to the axis. Manual markings of the start and the end of the blood vessel were used as starting point and minimization was performed using the steepest descent method. Then an ellipse was fitted through the measurement points as projected on the surface perpendicular to the fitted axis. Fitting was performed using the fit_ellipse function by O. Gal from the MathWorks depository, which uses a least-squares criterion. Some of the cells could not be fitted in this way, since the shape of the projected curves resembles a hyperbola instead of an ellipse. In these cases a hyperbola was fitted and subsequent analysis was performed in an analogous way. The hyperbola was fitted using the EllipseFitByTaubin by N. Chernov from the MathWorks depository, which is based on an algorithm developed by G. Taubin[70]. About 3% of all cells were fitted to both branches of a hyperbola, which impeded further analysis, so that these measurements were left out.

For some cells, the fit to the ellipse was not good enough to obtain reliable results. As measure for the quality of the fit we took the standard deviation of the residuals of the points on the curve and the points projected on the ellipse, relative to the distance of the projected point to the centre of the ellipse (S):

$$S = \sqrt{\frac{1}{n}\sum_{n}(d_1/d_2)^2} \quad (1)$$

where n is the number of points on the curve, d_1 is the distance between the point on the curve and the same point projected on the fitted ellipse, and d_2 is the distance of the projected point to the centre of the fitted ellipse. Cells with a value of S higher than 0.1 were discarded for analysis, which corresponds to 18% of the unrolled cells. Changing this threshold to 0.13 had only minor effects on P values obtained. In that case, 11% of the unrolled cells were discarded. The fits on the hyperbola were all good enough for further analysis.

After fitting the ellipse or the hyperbola, measurement points were projected onto it. For the hyperbola the Residuals_hyperbola function by H. Ma from the MathWorks depository was used, which is an adaptation of an algorithm introduced by D. H. Eberly[71]. The ellipse or hyperbola was then unrolled, resulting in a two-dimensional cell shape. As a control for the procedure, the perimeter was calculated from this two-dimensional projection, as well as from the original measurement points by assuming straight lines between the points for the latter case. The mean difference between these values was 1.7%, thus providing validation for the procedure. Cell area was calculated from the two-dimensional projection using a standard equation for calculating polygon areas (http://mathworld.wolfram.com/PolygonArea.html), and cell elongation and orientation were obtained using the fit_ellipse function on this projection. Elongation was defined as the ratio of the long axis and the small axis minus 1 and the orientation is the tilting of the long axis.

To estimate the error arising from this procedure, the unrolling of the ellipse was also performed in a way to maximize the error: instead of projecting the measurement points on the ellipse and then unrolling this ellipse, the projection was not carried out and unrolling was performed for each point individually, using an ellipse that was resized to go through the measurement point. Analogously, for the hyperbola the major and minor axes were rescaled for each measurement point. For statistical analysis, the analysis error was taken into account by replacing the standard deviation (s.d.) by the following measure:

$$\text{s.d.}' = \sqrt{\text{s.d.}^2 + \frac{1}{n-1}\sum_{n}\left(a[i]-a'[i]\right)^2} \quad (2)$$

where n is the number of cells that are analysed, $a[i]$ is the calculated value of the ith cell and $a'[i]$ is the value that was obtained for the same cell in the alternative way.

Significance was determined using a Student's t-test with the adjusted standard deviation.

Code availability. All code used in this study is available from the authors on request.

Statistics and reproducibility. Unless explicitly stated, all results shown were obtained from 3 independent experiments, sample sizes were not predetermined, the experiments were not randomized and investigators were not blinded to allocation during experiments and outcome assessment.

Data availability. All data supporting the findings of this study are available from the corresponding author on reasonable request.

58. Westerfield, M. *The Zebrafish Book* (University of Oregon Press, 1993).
59. Allinson, K. R., Carvalho, R. L., van den Brink, S., Mummery, C. L. & Arthur, H. M. Generation of a floxed allele of the mouse Endoglin gene. *Genesis* **45,** 391–395 (2007).
60. Wang, Y. *et al.* Ephrin-B2 controls VEGF-induced angiogenesis and lymphangiogenesis. *Nature* **465,** 483–486 (2010).
61. Cermak, T. *et al.* Efficient design and assembly of custom TALEN and other TAL effector-based constructs for DNA targeting. *Nucleic Acids Res.* **39,** e82 (2011).
62. Villefranc, J. A., Amigo, J. & Lawson, N. D. Gateway compatible vectors for analysis of gene function in the zebrafish. *Dev. Dyn.* **236,** 3077–3087 (2007).
63. Bussmann, J. & Schulte-Merker, S. Rapid BAC selection for tol2-mediated transgenesis in zebrafish. *Development* **138,** 4327–4332 (2011).
64. Siekmann, A. F. & Lawson, N. D. Notch signalling limits angiogenic cell behaviour in developing zebrafish arteries. *Nature* **445,** 781–784 (2007).

65. Mori, N. & Chang, K. *PIV toolbox in MATLAB-Getting Started with mPIV* (2004).
66. Hove, J. R. *et al*. Intracardiac fluid forces are an essential epigenetic factor for embryonic cardiogenesis. *Nature* **421,** 172–177 (2003).
67. Anton, H. *et al*. Pulse propagation by a capacitive mechanism drives embryonic blood flow. *Development* **140,** 4426–4434 (2013).
68. Fåhræus, R. & Lindqvist, T. The viscosity of the blood in narrow capillary tubes. *Am. J. Physiol.* **96,** 562–568 (1931).
69. Goetz, J. G. *et al*. Endothelial cilia mediate low flow sensing during zebrafish vascular development. *Cell Rep.* **6,** 799–808 (2014).
70. Taubin, G. Estimation of planar curves, surfaces, and nonplanar space-curves defined by implicit equations with applications to edge and range image segmentation. *IEEE Trans. Pattern Anal.* **13,** 1115–1138 (1991).
71. Eberly, D. H. *3D Game Engine Design: A Practical Approach to Real-time Computer Graphics* 2nd edn (Morgan Kaufmann Publishers, 2007).

nature cell biology

DOI: 10.1038/ncb3528

In the format provided by the authors and unedited.

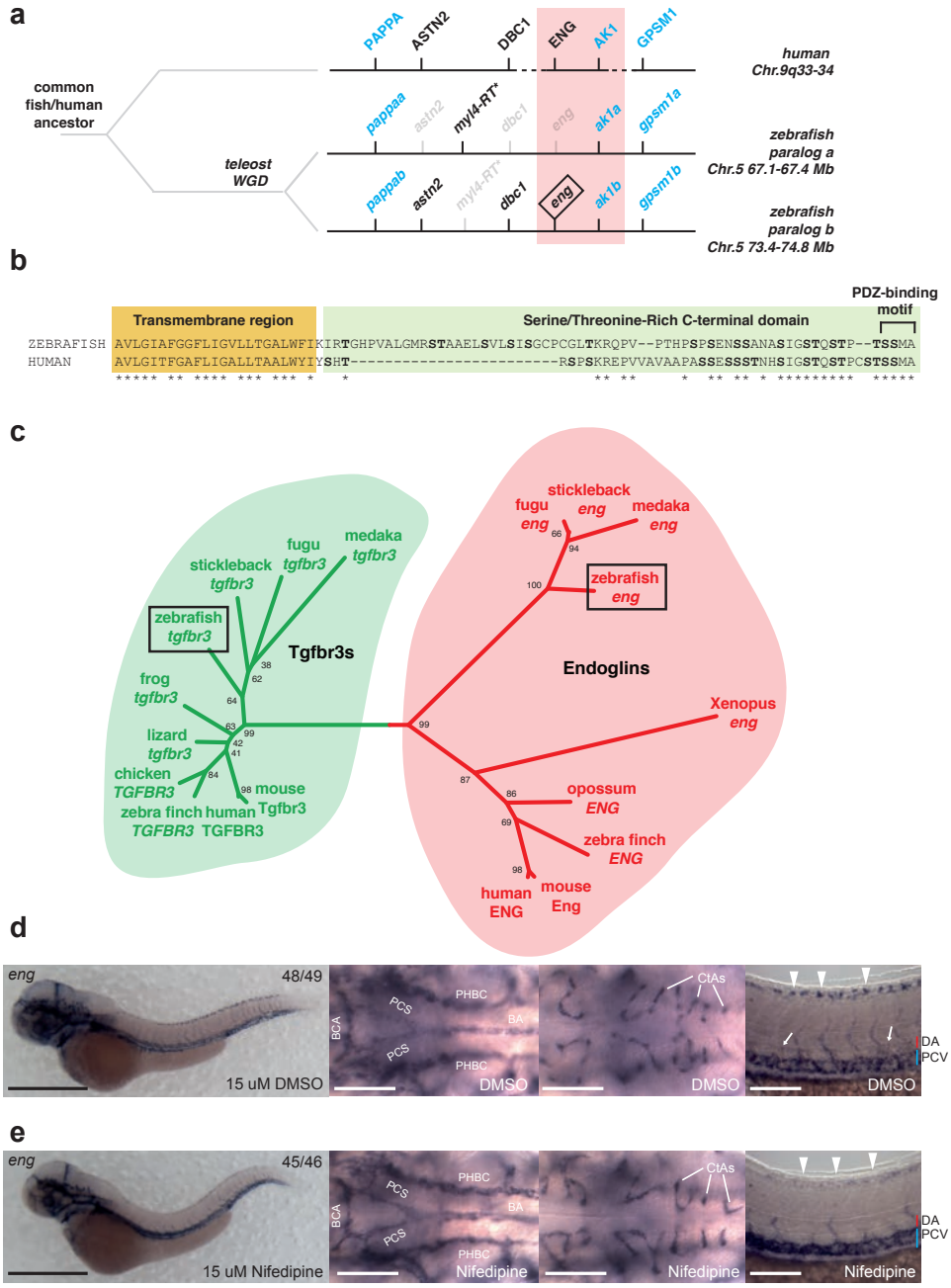

Supplementary Figure 1 Identification of a zebrafish *endoglin* orthologue. **(a)** Schematic representation of the endoglin locus showing conservation of gene order (synteny) between human chromosome 9q33-34 and two paralogous loci on zebrafish chromosome 6 containing the Pregnancy-associated plasma protein A (*pappa*), Astrotactin 2 (*astn2*), a retrotransposed Atrial myosin light chain (*myl4-RT*), Deleted in bladder cancer 1 (*dbc1*), *endoglin* (*eng*), *adenylate kinase 1* (*ak1*) and G-protein signaling modulator 1 (*gpsm1*) genes. Paralogous genes that were likely duplicated during the teleost whole genome duplication (WGD) event are indicated in blue. Subsequent gene loss on the paralogous chromosomes (lost genes in grey) most likely resulted in the current gene order. Pink shading indicates a small synteny block containing the Endoglin and AK1 genes. Dashed lines indicate synteny breaks between human and zebrafish. **(b)** Alignment of the conserved C-terminal region of zebrafish and human Endoglin. Asterisks indicate conserved residues. **(c)** Phylogenetic tree based on the alignment of the C-terminal sequences (transmembrane region and C-terminal domain) of vertebrate Tgfbr3 (green shading) and Endoglin (red shading). Numbers at branchpoints represent bootstrap values (percentage out of 1000 replicates). **(d)** Whole-mount *in situ* hybridization of *eng* shows vascular-restricted expression in 52 hpf zebrafish embryos. Expression is detected in the basal communicating artery (BCA), the posterior communicating segments (PCS), basilar artery (BA), primordial hindbrain channels (PHBC) and central arteries (CtAs) of the hindbrain as well as the dorsal aorta (DA, arrows), posterior cardinal vein (PCV) and dorsal longitudinal anastomotic vessel (DLAV, arrowheads) of the trunk vasculature. Scale bar in overview picture is 500 um, in high magnification images scale bar is 100 um. Images are representative of 48 out of 49 embryos. **(e)** Whole-mount *in situ* hybridization of *eng* expression in WT embryos treated with 15 uM nifedipine from 48-52 hpf. Note that blood flow reduction does not affect hindbrain expression, but decreases *eng* mRNA levels in the DLAV (arrowheads). Scale bar in overview picture is 500 um, in high magnification images scale bar is 100 um. Images are representative of 45 out of 46 embryos.

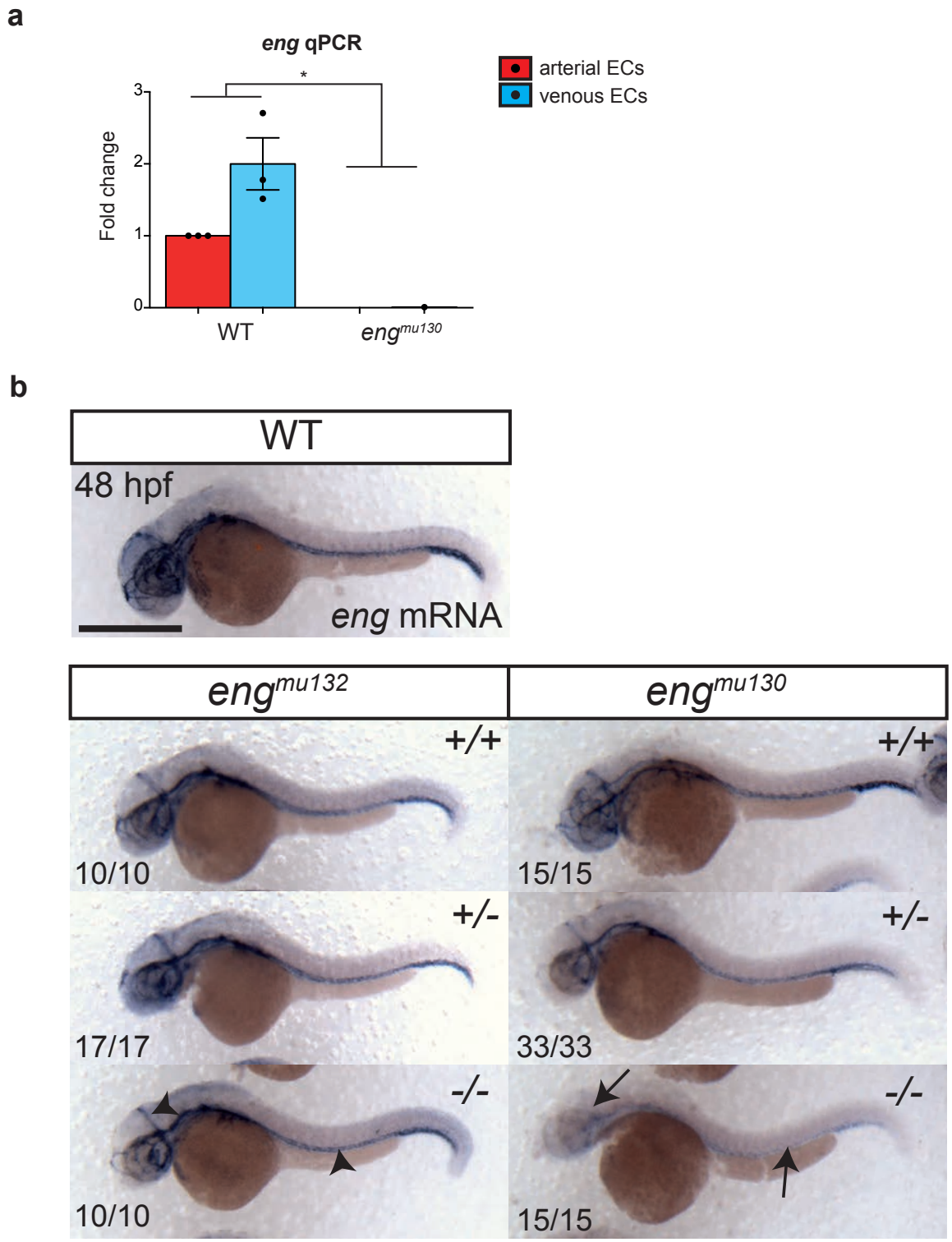

Supplementary Figure 2 *eng* mRNA is subject to nonsense-mediated decay in *eng*^{mu130} mutants. **(a)** qPCR to detect zebrafish *eng* in FACS-sorted arterial and venous ECs from pooled 72 hpf embryos. Data is shown as relative expression normalized to WT arterial EC levels. In WTs, *eng* transcript can be detected at similar levels in the arterial and venous populations, and is almost non-detectable in *eng*^{mu130} mutant ECs. Experiments were performed n=3 times independently and were analysed by paired Student's *t*-test. **(b)** Whole-mount *in situ* hybridization for *endoglin* expression at 32 hpf in embryos from WT, *eng*^{mu130} and *eng*^{mu132} heterozygous incrosses. All embryos carrying *eng*^{mu132} alleles (which contain a 7nt substitution that does not introduce a frameshift) show the same staining intensity as WT, with particularly strong expression in the PCV (arrowhead). *eng*^{mu130} +/- embryos already show decreased staining, which disappears almost entirely from the head and trunk vasculature in *eng*^{mu130} mutants (arrows). Scale bar is 500 um. Images are representative of the number of embryos as indicated in the respective panel. n.s., not significant, *P<0.05, **P<0.01, ***P<0.001, error bars indicate s.e.m.

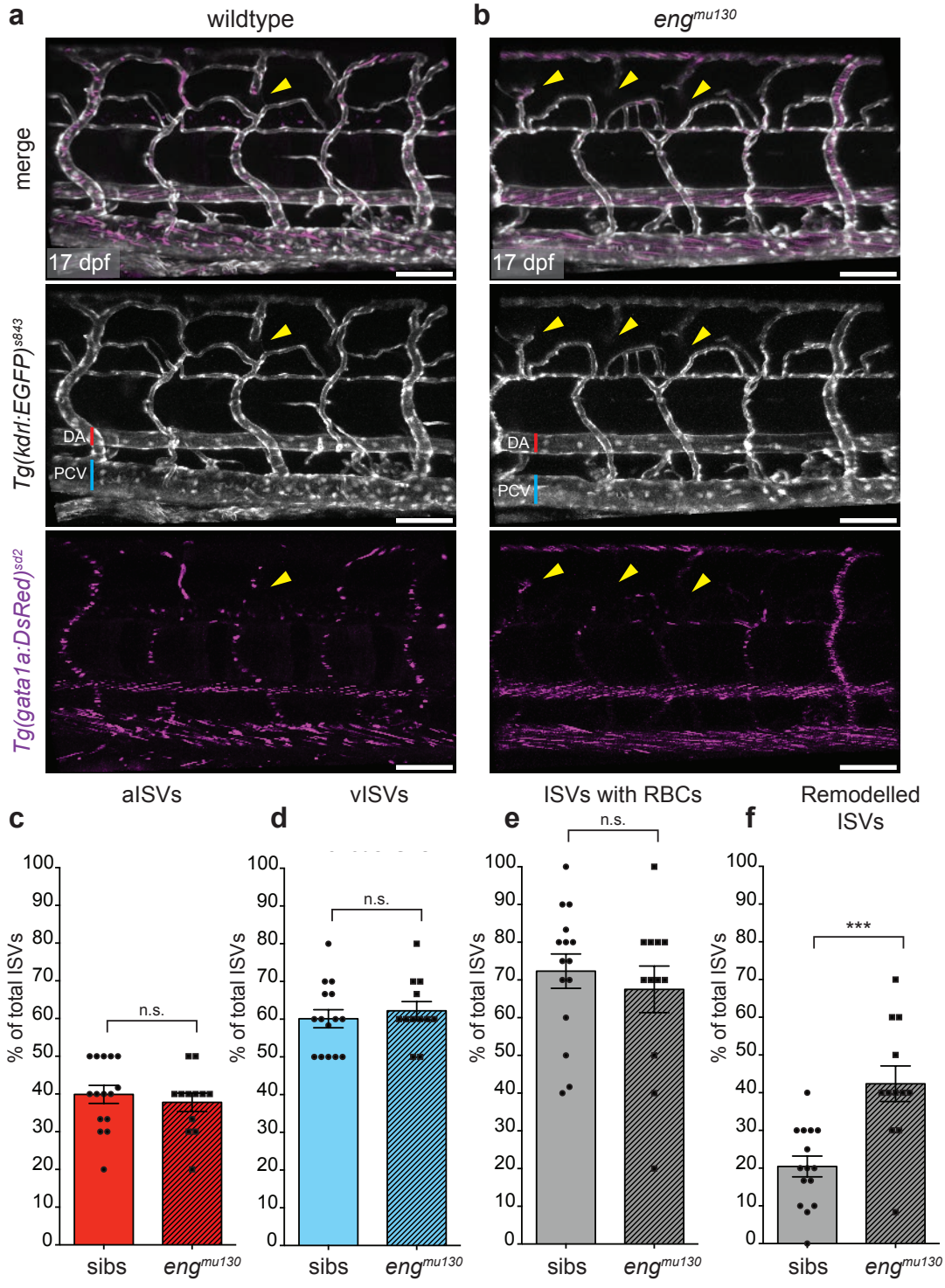

Supplementary Figure 3 ISV remodelling in WT and *eng*^{mu130} 17 dpf juveniles. **(a, b)** Maximum intensity projections of confocal z-stacks of 17 dpf WT **(a)** and *eng*^{mu130} mutants **(b)**. Yellow arrowheads point to remodelled ISVs that no longer maintain connection to the DLAV. Scale bar is 100 um. **(c-f)** Quantification of aISV identity **(c)**, vISV identity **(d)**, ISVs containing DsRed+ erythrocytes **(e)** and remodelled ISVs **(f)**. WTs and *eng*^{mu130} mutants have no difference in ISV distribution or presence of RBCs, but *eng*^{mu130} mutants show increased remodelling (n=15 siblings (158 ISVs analysed) and n=12 muts (122 ISVs analysed)). Analysed by unpaired Student's *t*-test. n.s., not significant, *P<0.05, **P<0.01, ***P<0.001, error bars indicate s.e.m.

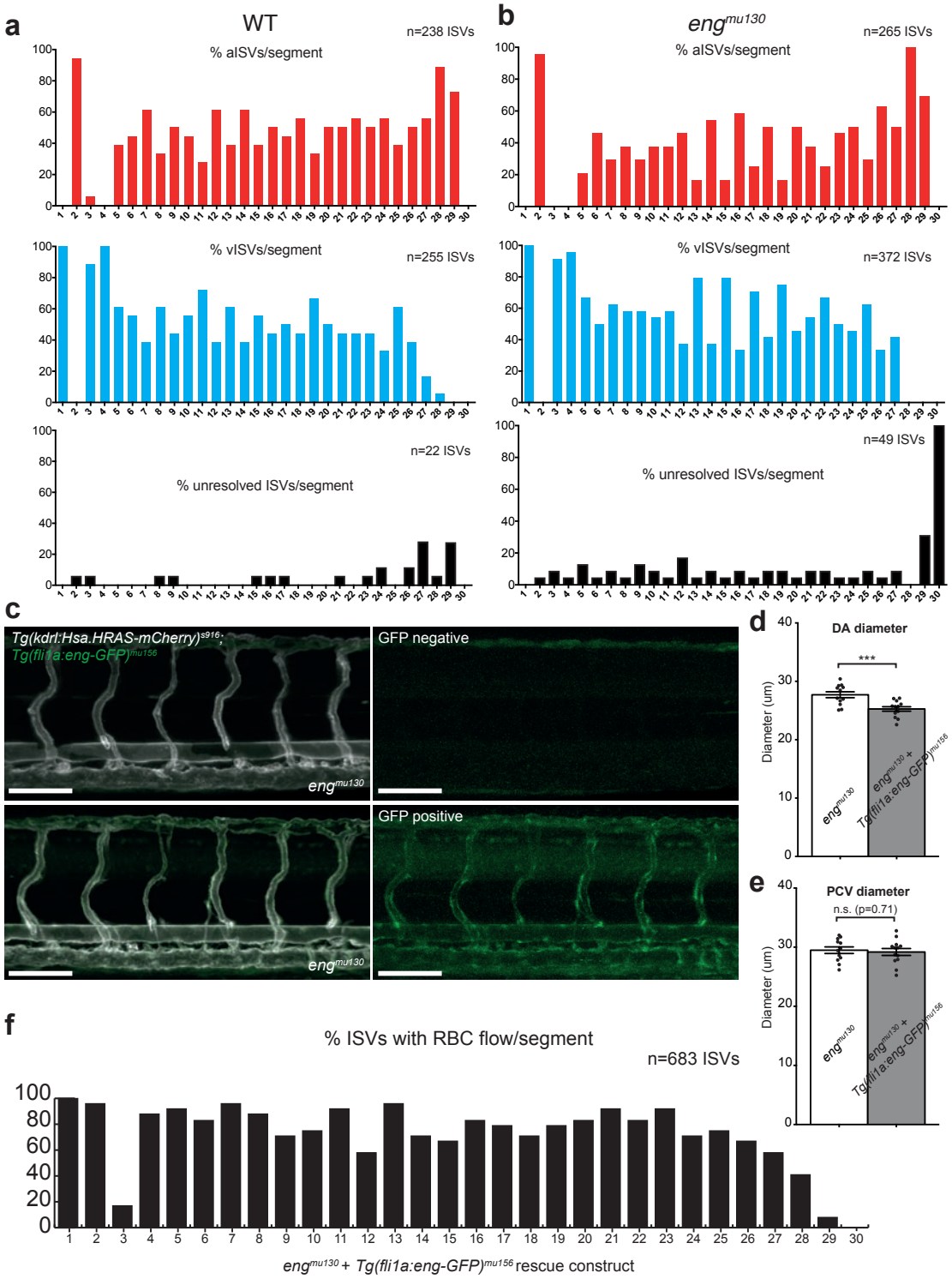

Supplementary Figure 4 Arterial-venous specification is unaffected in *endoglin* mutants. **(a, b)** Arterial-venous identity of ISVs as determined by flow direction and/or morphology (connection to DA or PCV) in WTs and *eng*^{mu130} mutants. WTs and mutants have similar distribution of arteries and veins, with a slight increase in the number of unresolved ISV connections in *eng*^{mu130} mutants. Indicated numbers of ISVs from 9 WT and 12 mut embryos were analysed. **(c)** Maximum intensity projection of confocal z-stack of *eng*^{mu130} mutants at 72 hpf. *Tg(fli1a:eng-GFP)*^{mu156} embryos exhibit vascular-specific GFP expression, evidenced by overlap with *Tg(kdrl:Hsa.HRAS-mCherry)*^{s916}. Scale bar is 100 um. **(d, e)** Quantification of DA **(d)** and PCV **(e)** diameters in *eng*^{mu130} mutants with or without the *Tg(fli1a:eng-GFP)*^{mu156} rescue construct. Tagged endoglin-GFP modestly rescues DA, but not PCV diameters (n=12 GFP-negative, n=13 GFP-positive *eng*^{mu130} mutants). Analysed by unpaired Student's *t*-test. **(f)** Quantification of the number of ISVs actively carrying RBCs shows rescue in *eng*^{mu130} embryos carrying the *Tg(fli1a:eng-GFP)*^{mu156} rescue construct. 683 ISVs from 13 GFP-positive *eng*^{mu130} mut embryos were analysed. n.s., not significant, *P<0.05, **P<0.01, ***P<0.001, error bars indicate s.e.m.

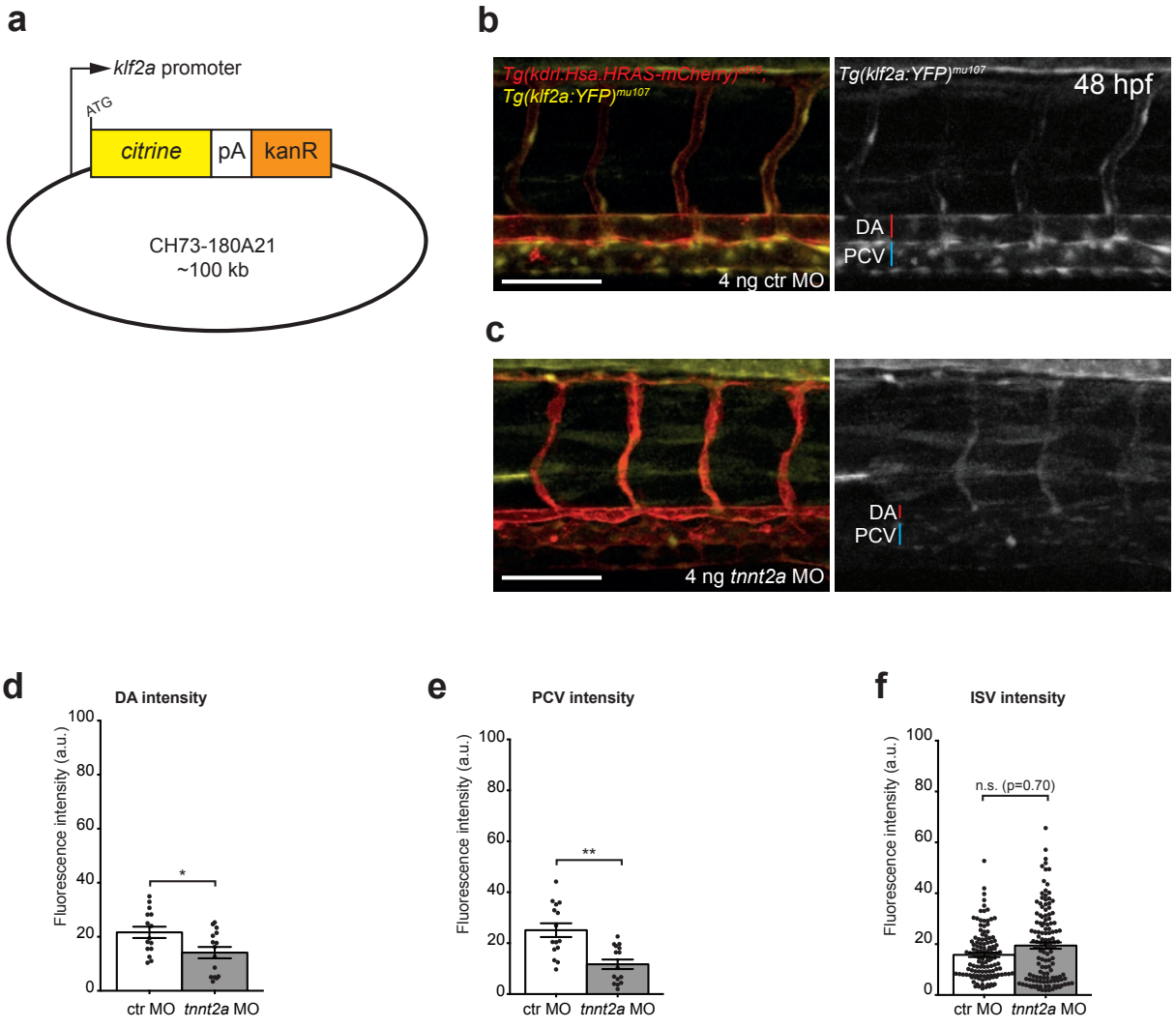

Supplementary Figure 5 Generation of the *Tg(klf2a:YFP)*^{mu107} reporter line. **(a)** Schematic of the cloning strategy. A Citrine cassette was inserted behind the endogenous ATG of the *klf2a* gene contained in the CH73-180A21 BAC by homologous recombination. **(b, c)** *Tg(klf2a:YFP)*^{mu107} embryos display vascular-specific YFP expression, evidenced by overlap with *Tg(kdrl:Hsa.HRAS-mCherry)*^{s916}. Embryos treated with *tnnt2a* MO lose YFP expression in the DA and PCV. Scale bar is 100 um. **(d-f)** Quantification of YFP fluorescence intensity in the DA, PCV and ISVs in ctr MO and *tnnt2a* MO injected embryos (DA/PCV: n=15 control MO, n=15 *tnnt2a* MO; ISVs: n=126 ISVs from 15 control MO, n=133 ISVs from 15 *tnnt2a* MO). Analysed by Mann-Whitney *U* test. n.s., not significant, *P<0.05, **P<0.01, ***P<0.001, error bars indicate s.e.m.

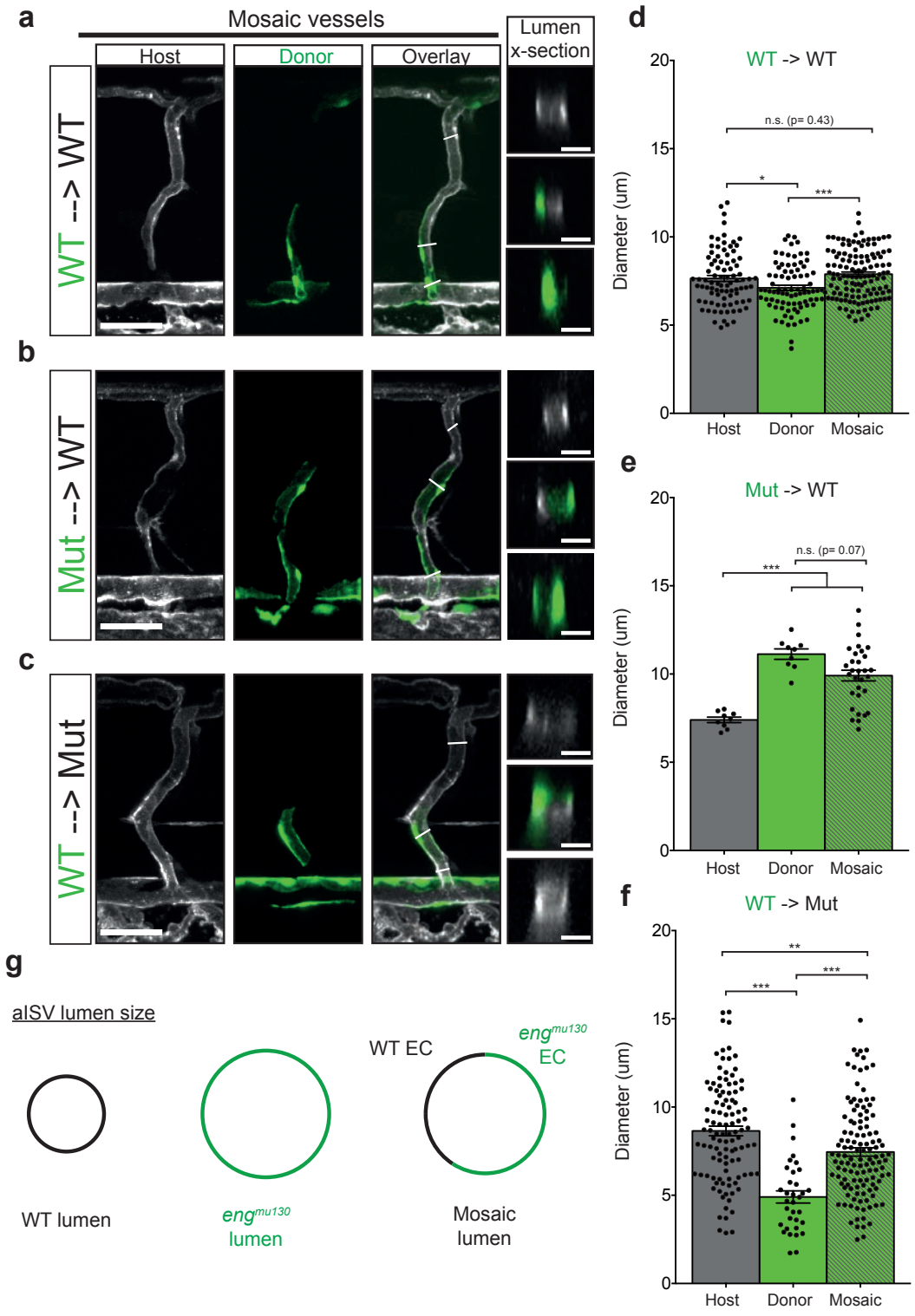

Supplementary Figure 6 Transplantation analysis of mosaic ISVs. **(a-c)** Maximum intensity projections of confocal z-stack of mosaic ISVs from **(a)** WT->WT, **(b)** Mut->WT and **(c)** WT->Mut transplantations. Optical sections reveal portions of lumen comprised only of donor cells, only of host cells, or a mosaic combination of host and donor cells. Scale bar on overview is 50 um, scale bar on lumen cross-section is 10 um. **(d-f)** Quantification of mosaic ISV diameters depending on cellular composition from **(d)** WT->WT, **(e)** Mut->WT and **(f)** WT->Mut transplantations. All ISVs from WT->WT transplantations had normal diameters **(d)**, while mutant cells caused dilation when they formed part or all of the lumen in Mut->WT situations **(e)**. WT cells were able to reduce ISV diameter when they formed all of the lumen in WT->Mut scenarios (**f**). (WT->WT n= 216 vessel segments from 54 ISVs; Mut->WT n=44 vessel segments from 11 ISVs; WT->Mut n=204 vessel segments from 51 ISVs). Analysed by One-Way ANOVA. **(g)** Schematic summarizing the requirement for *eng* function in every cell of a vascular tube to maintain proper dimensions. n.s., not significant, *P<0.05, **P<0.01, ***P<0.001, error bars indicate s.e.m.

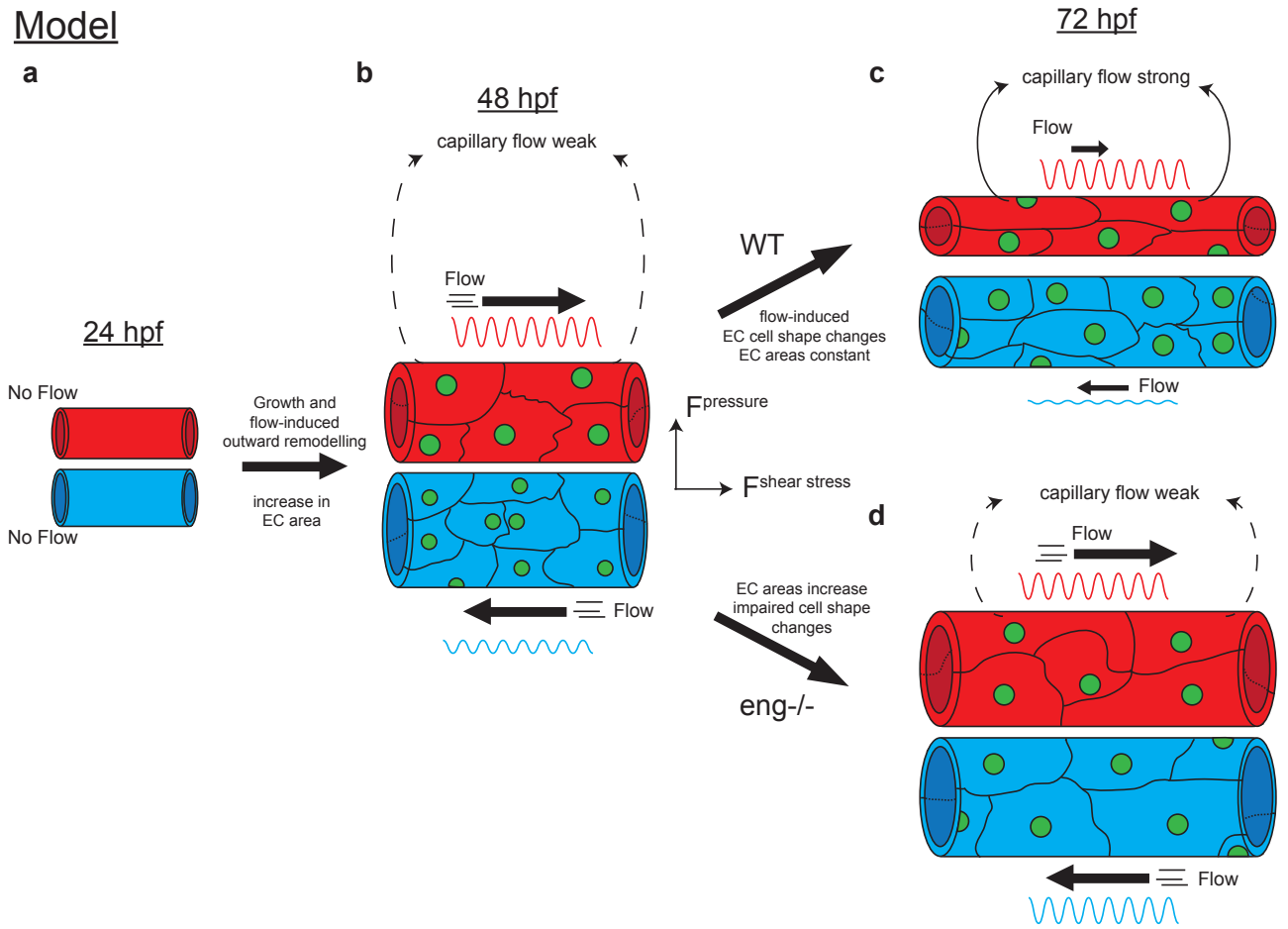

Supplementary Figure 7 Model for endoglin's role in the biphasic response of ECs to blood flow. **(a)** By 24 hpf, the first artery and vein have assembled by vasculogenesis. Blood flow starts. **(b)** As development proceeds, cardiac output rises. The axial vessels increase in diameter and carry an increasing volume of blood. At 48 hpf, the capillaries connecting the artery and vein have just begun to lumenize and carry flow. **(c)** Between 48 and 72 hpf, blood flow triggers shape changes in WT ECs. They elongate and align in the direction of flow, without changing their surface areas. This lengthens the vessel and reduces its diameter. The arterial constriction redirects blood flow through the capillary network. **(d)** In *eng*-deficient blood vessels, ECs are unable to limit their surface areas in response to blood flow. Although elongation still occurs to some extent, the increase in size impedes the ability of ECs to align to the flow. Ultimately, this results in vessel dilation and the formation of an arterio-venous shunt. The high velocities achieved in the shunt prevent RBCs from passing into capillaries, and the pulsatile quality of arterial flow is transmitted to the venous return.

Original blot scans used in Figure 5e

ENG

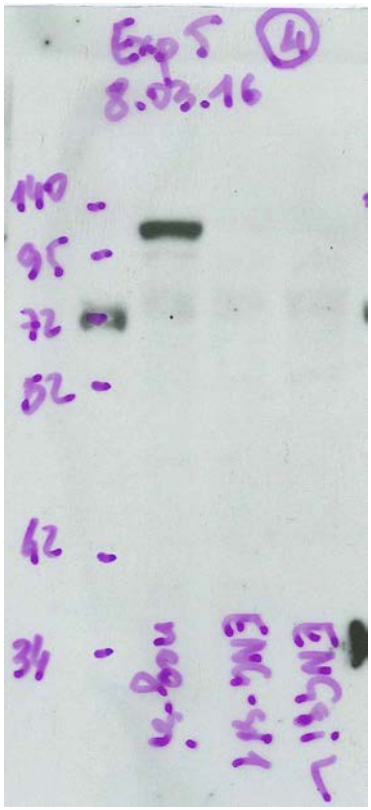

α-Tubulin

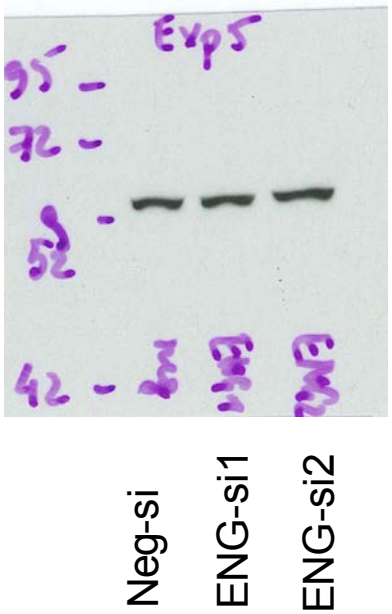

Supplementary Figure 8 Original scanned blots used in Figure 5e.

Supplementary Movie Legends

Supplementary Movie 1 Distal blood flow in WT fin regenerate at 5 dpa. Brightfield movie of blood flow in the distal regenerating fin of WT fish at 5 dpa. Numbers label individual bony rays. Arrows indicate flow direction, while dashed lines denote arteries (red) and veins (blue). Flow from a centrally located artery distributes through a plexus to two veins at the end of each ray. Note weak flow reversal in lateral vein of the first ray, arcing over an inactive artery.

Supplementary Movie 2 AVMs and disturbed flow in *eng*^{mu130} fin regenerate at 5 dpa. Brightfield movie of blood flow in the distal regenerating fin of *eng*^{mu130} mutant at 5 dpa. Numbers label individual bony rays. Arrows indicate flow direction, while dashed lines denote arteries (red) and veins (blue). Note prominent AVMs in second ray from the left. In ray #3, more proximally located AVMs either stop or reverse blood flow in the veins, and the central artery is not active. Ray #4 has strong flow reversal in the left vein, arcing over an inactive central artery. Note bleedings at distal end of all rays.

Supplementary Movie 3 ISV flow in 72 hpf sibling embryo. Brightfield movie of RBC flow in the trunk of sibling embryo at 72 hpf. Nearly all ISVs on both sides of the embryo carry RBC flow.

Supplementary Movie 4 ISV flow in 72 hpf *eng*^{mu130} embryo. Brightfield movie of RBC flow in the trunk of *eng*^{mu130} embryo at 72 hpf. Note that only 1 or 2 ISVs have persistent RBC flow, while most have no or only very intermittent RBC flow.

Supplementary Movie 5 Optical rail restores RBC flow in capillaries of *eng*^{mu130} mutants. Brightfield movie of RBC flow in the trunk of *eng*^{mu130} embryo at 72 hpf. Holographic optical tweezers (HOT) are focused at entrance to an aISV, but laser is turned off. About halfway through movie the laser is turned on (red circle indicates HOT focal point), slows down RBCs that pass through the laser, and diverts them from the main arterial blood flow into the capillary.

Supplementary Movie 6 Time-lapse of cell shape changes in DA between 48-72 hpf in sibling embryo. Maximum intensity projection of confocal z-stacks of *Tg(fli1a:lifeactEGFP)*^{mu240}*; Tg(fli1a:nEGFP)*^{y7}, and *Tg(-0.8flt1:RFP)*^{hu5333} in sibling embryo between 48-72 hpf. Acquisitions were made at 40 min intervals, shown at 5 frames per second. Note decrease in DA diameter between 48-72 hpf, and elongation of ECs.

Supplementary Movie 7 Time-lapse of cell shape changes in DA between 48-72 hpf in *eng*^{mu130} embryo. Maximum intensity projection of confocal z-stacks of *Tg(fli1a:lifeactEGFP)*^{mu240}*; Tg(fli1a:nEGFP)*^{y7}, and *Tg(-0.8flt1:RFP)*^{hu5333} in *eng*^{mu130} embryo between 48-72 hpf. Acquisitions were made at 40 min intervals, shown at 5 frames per second. Note a similar DA diameter at 48 hpf as sibling in Supplementary Movie 4 that fails to decrease appreciably by 72 hpf. Note, additionally, the dramatic increase in EC sizes compared to siblings during the movie.